nature water

Supplementary information

https://doi.org/10.1038/s44221-026-00700-2

Solar-powered resource separator for clean water production, electricity generation and critical resource recovery

In the format provided by the authors and unedited

Table of Contents

1 Supplementary Methods

1.1 Materials and Reagents

Chlorella powder, nonwoven fabric, PV panels, carbon felt, aluminum foil, and waterproof glue are purchased from the Alibaba platform (China). Tris(hydroxymethyl)aminoethane buffer (Tris buffer, pH ≈ 8.5) and uranium nitrate ($UO_2(NO_3)_2 \cdot 6H_2O$, ≥99.8%) are from Macklin Biochemical Co., Ltd (Shanghai, China). Polyethyleneimine (99%, Mw:10,000) and dopamine hydrochloride (98%) are bought from Aladdin Biochemical Co., Ltd (Shanghai, China). SYTO 9 Green Fluorescent Nucleic Acid Stain (SYTO9) is purchased from Shanghai Fushen Biotechnology Co., Ltd. (Shanghai, China). Other regents are all purchased from Sinopharm Chemical Reagent Co., Ltd (Shanghai, China). All chemicals are of analytical grade and are used directly without further purification.

1.2 The fabrication of PPC

PPC is synthesized through Mussel-inspired synthesis and Michael addition reaction[1]. Typically, 5.0 g of Enteromorpha is calcined at 600 °C for 3 hours under a N_2 atmosphere. The resulting product is washed with deionized water and dried at 70 °C under vacuum to obtain the precursor of PPC. Subsequently, 1.0 g of this precursor, 1.0 g of dopamine hydrochloride, and 1.2 g of polyethyleneimine are added to 0.4 L of Tris buffer (pH ≈ 8.5). The mixture is stirred for 24 hours, after which the PPC is collected, washed with deionized water, and dried at 70 °C under vacuum.

1.3 The fabrication of HMO

HMO is synthesized according to a previously reported method[2, 3]. Typically, the precursor is prepared by calcining a mixture of $MnCO_3$ and Li_2CO_3 (with a Li/Mn molar ratio of 1.33:1.67) at 500 °C for 4 h in air. Subsequently, Li^+/H^+ ion exchange is carried out by treating the precursor in 0.5 M HCl solution for 24 h. HMO is then obtained after being washed with deionized water until the pH of the supernatant reaches approximately 7.0, and dried at 70 °C under vacuum.

1.4 Characterization

The morphologies are characterized by scanning electron microscopy (SEM, ZEISS Gemini SEM 300, Germany), with the accompanying Energy-dispersive X-ray spectroscopy (EDS) used to qualitatively analyse the elements contained in the sample surface. The surface functional groups are measured by Fourier Transform Infrared Spectrometer (FT-IR, Thermo Scientific Nicolet iS10, USA) with a sweep wavenumber range of 400-4000 cm^{-1}. The chemical compositions are characterized by X-ray photoelectron spectroscopy (XPS, Thermo Scientific K-Alpha, USA). The structural characteristics are characterized by X-ray diffraction (XRD, Rigaku Ultima IV, Japan). The optical absorption is measured by Ultraviolet-Visible-Near-Infrared (UV-Vis-NIR) spectrophotometer (Shimadzu UV-3600, Japan) over a wavelength ranging from 300 to 2500 nm. The water contact angle is characterized by a surface tension-contact angle meter (SL200B, Solon Tech, USA). The evaporation enthalpy is determined by a differential scanning calorimeter (DSC, TA DSC25, USA). The water existing state in SAU or SALi is characterized by Raman spectroscopy, and a laser with a wavelength of 514 nm is used (Horiba LabRAM HR Evolution, Japan). Nitrogen adsorption-desorption isotherms are obtained by using a fully automated surface area and porosity analyzer (Quantachrome Autosorb IQ, USA). Before analysis, all samples are degassed under vacuum to remove physically adsorbed species. The specific surface area is calculated using the Brunauer-Emmett-Teller (BET) method, and pore size distributions are derived from the adsorption branch using density functional theory (DFT). The mechanical properties are tested by a microcomputer-controlled electronic universal testing machine (SANS CMT5105, China). Thermogravimetric analysis (TGA) is conducted using a thermogravimetric analyzer (NETZSCH STA 449 F5 Jupiter, Germany) under a nitrogen atmosphere. The total organic carbon (TOC) of the condensed water is measured by a TOC analyzer (MULTI N/C 3100, Analytik Jena, Germany). The total dissolved solids (TDS) of the condensed water are measured by a TDS meter (SevenCompact S230, Mettler Toledo, Switzerland). pH is measured using a pH meter (SevenCompact S210, Mettler Toledo, Switzerland).

1.5 Solar-driven multi-product extraction experiments

To prevent cross-interference among the extraction of multiple products, the indoor multi-product extraction experiments are conducted independently. For indoor water production and electricity generation experiments, unless special statements, all studies are conducted with the PV panel of ~20 cm^2. The compositions of the inlet tank for the solar-driven multi-product extraction experiments are summarized as follows:

Experiments	Inlet tank
PV cooling	Deionized water
Solar-driven clean water production	Deionized water
Solar-driven uranium extraction	2.5 mg L^{-1} of uranium solution
Solar-driven lithium extraction	2.5 mg L^{-1} of lithium solution

For indoor adsorption experiments, unless special statements, all studies are conducted with the SAU or SALi of 4 cm^2 with a contact time of 0.1-48 h, and the ion concentration ranges from 2.5 to 20 mg L^{-1} at constant stirring (200 rpm). pH value is adjusted by HCl and NaOH, respectively. The Langmuir model (**Eq. S1**) and Freundlich model (**Eq. S2**) can be expressed as follows[4]:

$$q_e = \frac{q_m K_L C_e}{1 + K_L C_e} = \frac{q_m C_e}{K_L^{-1} + C_e} \quad \text{(S1)}$$

$$q_e = K_F C_e^{1/n_f} \quad \text{(S2)}$$

Where q_m is the theoretical maximum adsorption capacity (g g^{-1}); K_L is the constant of the Langmuir model (L mg^{-1}). K_F and $1/n_f$ are the Freundlich constants representing the adsorption capacity and adsorption intensity, respectively.

The cyclic experiments are conducted continuously for 20 cycles, with each cycle lasting 2 days. During each cycle, brine is added to the inlet tank every 12 h to ensure a sufficient brine supply, while the solution in the outlet tank is simultaneously removed to prevent overflow. The compositions of the inlet tank for different cyclic experiments are summarized as follows:

Cyclic experiment	Inlet tank composition
Clean water production	Real seawater (collected from the South China Sea)
Uranium extraction	Real seawater spiked with 2.5 mg L^{-1} uranium ion
Lithium extraction	Real seawater spiked with 2.5 mg L^{-1} lithium ion

The performance testing procedure follows the same protocol described above. For cyclic lithium extraction, SALi is regenerated using 0.1 M HCl as the eluent after adsorption saturation, whereas for cyclic uranium extraction, SAU is regenerated using 0.1 M Na_2CO_3. In both cases, the elution time is 24 h. The yield (Y) of the obtained products (lithium salt and uranium product) is calculated based on the **Eq. S3** where q_d and q_a was desorbed amount and adsorbed amount.

$$Y = \frac{q_d}{q_a} \tag{S3}$$

The purity (P_{op}) of the obtained product is calculated based on **Eq. S4** where C_{tar} and C_{all} are the target ion concentration and total ion concentration in the elution solution.

$$P_{op} = \frac{C_{tar}}{C_{all}} \tag{S4}$$

1.6 Performance comparison and versatility test.

For the performance comparison in **Fig. 3h**, most performance data come from the original literature. For LTO@NMC[5], n-HTO[6], anti-hydrogel[7], and GDH[8], we synthesize these materials and measure their equivalent adsorption capacity (unit is mg m^{-2} instead of mg g^{-1}).

For the adsorbents in **Supplementary Fig. 38**, they are synthesized according to the reported method (GDH[8], and HR-COFs[9]). The corresponding six-stage ASP is prepared according to *Method* Section in the text**.**

For the adsorbents in **Supplementary Fig. 39**, they are synthesized according to the reported method (boron[10] and cesium[11]). The corresponding six-stage ASP is prepared according to *Method* Section in the text**.**

1.7 COMSOL simulations

A transient model is employed to study the salt distribution in capillary evaporation wick. The details can be found in our reported works[12]. The concentration ratio (CR) is calculated based on **Eq. S5** where C_{ic} and C_{oc} are inlet and outlet concentrations, respectively.

$$CR = \frac{C_{oc}}{C_{ic}} \tag{S5}$$

The geometric model is shown below. The length and thickness of the simulated domain are 10 cm and 1 cm, which include the size of the lab-scale ASP.

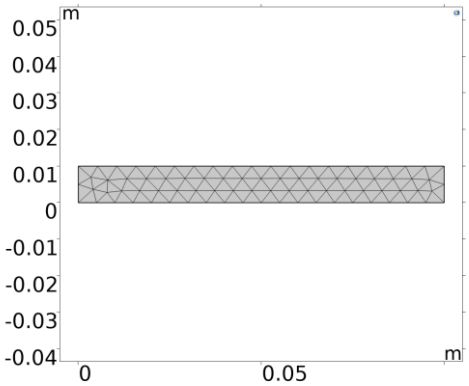

2 Supplementary Note

2.1 TOPSIS method

TOPSIS is a multi-criteria decision-making method to rank alternatives based on their distances to the ideal and anti-ideal solutions[13]. Although TOPSIS is not specifically developed for adsorbent design, it has been widely applied in engineering optimization, materials selection, and environmental decision-making problems, where multiple conflicting criteria must be considered simultaneously[14, 15, 16]. We use TOPSIS here owing to its simplicity, transparency, and ability to quantitatively integrate multiple performance indicators without requiring extensive subjective assumptions. Compared with some other multi-criteria decision-making methods, TOPSIS provides an intuitive geometric interpretation based on proximity to the ideal solution, making it particularly suitable for systematically comparing adsorbents across multiple normalized criteria[17]. Assuming that "*m*" solutions and "*n*" evaluation indicators, the initial decision matrix can be obtained:

$$\mathbf{X}=\begin{bmatrix} x_{11} & \cdots & x_{1n} \\ \vdots & \ddots & \vdots \\ x_{m1} & \cdots & x_{mn} \end{bmatrix} \tag{S6}$$

Where x_{ij} is the original value of the "*i*" solution on the "*j*" indicator.

The decision matrix (**R**) is normalized by vector normalization method as follows:

$$r_{ij}=\frac{x_{ij}}{\sqrt{\sum_{k=1}^{m} x_{ij}^{2}}} \tag{S7}$$

$$\mathbf{R} = [r_{ij}]_{m\times n} \tag{S8}$$

The weight vector (**W**)= (w_1, w_2, w_n) (**W** satisfied $\sum_{j=1}^{n} w_j = 1$) is introduced to calculate the weighting matrix (**V**):

$$v_{ij} = w_j \cdot r_{ij} \tag{S9}$$

$$\mathbf{V} = [v_{ij}]_{m\times n} \tag{S10}$$

The Euclidean distance from solution "*i*" to the positive ideal solution (D_i^+) is calculated

as follows:

$$D_i^+ = \sqrt{\sum_{j=1}^{n} (v_{ij}\text{-}v_j^+)^2} \tag{S11}$$

$$v_j^+ = \begin{cases} \max(v_{1j}, v_{2j}, \ldots v_{mj}) \text{ for benefit indicators} \\ \min(v_{1j}, v_{2j}, \ldots v_{mj}) \text{ for cost-based indicators} \end{cases} \tag{S12}$$

The Euclidean distance from solution "*i*" to the negative ideal solution (D_i^-) is calculated as follows:

$$D_i^- = \sqrt{\sum_{j=1}^{n} (v_{ij}\text{-}v_j^-)^2} \tag{S13}$$

$$v_j^- = \begin{cases} \min(v_{1j}, v_{2j}, \ldots v_{mj}) \text{ for benefit indicators} \\ \max(v_{1j}, v_{2j}, \ldots v_{mj}) \text{ for cost-based indicators} \end{cases} \tag{S14}$$

The relative closeness of each solution (C_i) is calculated as follows:

$$C_i = \frac{D_i^-}{D_i^+ + D_i^-} \tag{S15}$$

The maximum C_i means the optimal solution. For uranium adsorbents and lithium adsorbents selective, adsorption capacity and cycling adsorption ratio are selected as "benefit indicators", and equilibrium time is selected as "cost-based indicators".

The pre-selected uranium adsorbents are shown below:

Uranium adsorbent	**Uranium adsorbent**	**Uranium adsorbent**
RGO-PDA/oxime[18]	Nb_3C_4@UiO-66-NH_2-PA[19]	CMC-PA-8[20]
rGO/LDH[21]	Fe_3O_4@Ti_3C_2-NH_2-PT[22]	GOG-RE[23]
PHCPs[24]	PA-MIL-101@MWCNT[25]	NENP-1[26]
APGO[27]	GO-pDA-PEI[28]	HNU-50[29]
CMNSC-Pro[30]	MB[31]	CSAOCF[32]
Porous MXene[33]	Fe_3O_4/CFA[34]	MIL-101-Cys[35]
TMP-g-AO[36]	Fe_3O_4@SiO_2[37]	EEA-AO[38]
TPP-DFP[39]	MSD[40]	AIC[41]
MCFCP[42]	AOPAN[43]	

The pre-selected lithium adsorbents are shown below:

Lithium adsorbent	Lithium adsorbent	Lithium adsorbent
$Li_{1.33}Fe_xMn_{1.67-x}O_4$[44]	HMO nanorods[45]	HMO-4%Mg[46]
HTO-P[47]	HMO spherical[48]	HMO-4%Al[46]
H_xTiO_3[49]	HMO-R[50]	HMO[46]
HTO-4[51]	HMO-S[50]	LFMO-0.05[52]
HTO-400[53]	HMO-F[50]	MIL-121-H_x[54]
HTO[55]	HMO-3D[50]	Li/Al-LDHs[56]
HTO-IV[57]	HMACO-0.04[58]	LIPs[59]
CAC-$Mn_{0.2}$[60]	HMO-L[61]	LMO[62]
Ni*x*-MnO2/BC[63]	$H_4Mn_5O_{12}$[64]	

2.2 The characterization of SAU and SALi

Compared to the commercial carbon felt (**Supplementary Fig. 6a**), the pores of SAU and SALi are filled by their respective gels; that is, PPC-doped sodium alginate gel for SAU (**Supplementary Fig. 6b**) and HMO-doped sodium alginate gel for SALi (**Supplementary Fig. 6c**). Elemental mapping analysis confirms the homogeneous distribution of key elements (nitrogen (N) and manganese (Mg) for PPC and HMO, respectively), indicating uniform dispersion of the above adsorbents inside (**Supplementary Fig. 7**). Fourier-transform infrared spectroscopy (FTIR) spectra of PPC and SAU are shown in **Supplementary Fig. 8**. For PPC (**Supplementary Fig. 8a**), the peaks at about 1082 and 1422 cm^{-1} are associated with C-N[65, 66]. The peaks around 1460 and 1498 cm^{-1} can be attributed to C=C vibration[67] and N-H vibration[68], respectively. The peaks at about 1389 and 1583 cm^{-1} are associated with nitrogen doping[69] and ring vibrations of PDA[70]. In comparison, characteristic peaks corresponding to PPC are largely absent on the SAU surface (**Supplementary Fig. 8b**), probably caused by the effective encapsulation by the sodium alginate gel matrix. The large peak at about 3438 cm^{-1} is indexed to the -OH stretching of sodium alginate gel in SAU[71]. X-ray photoelectron spectroscopy (XPS) analysis (**Supplementary Fig. 9**) further corroborates the chemical state and surface functional groups of SAU. The C1*s* peak can be divided into 284.3, 286.0, and 287.6 eV, indexed to C-C, C-O, and C=O, respectively (**Supplementary Fig. 9b**)[72, 73]. The O1*s* peak can be fitted by two peaks at around 532.4 and 530.5 eV, indexed to C-O and C=O, respectively (**Supplementary Fig. 9b**)[73]. Finally, X-ray diffraction (XRD) patterns provide definitive evidence for the presence of HMO in SALi (**Supplementary Fig. 10**). The water contact angle measurements show that a 3 μL water droplet is instantaneously absorbed upon the surface of either SAU or SALi (**Supplementary Fig. 11**), demonstrating their strong hydrophilic nature.

2.3 Evaporation performance of ASP

Compared to the pure water system (0.33 kg m^{-2} h^{-1}), the single-stage SAU-based ASP exhibits a higher evaporation flux (1.77 kg m^{-2} h^{-1}) under 1 sun irradiation (**Supplementary Fig. 16a**), while the SALi-based ASP demonstrates a similar evaporation performance (**Supplementary Table 2**). Both SAU and SALi possess low evaporation enthalpies of 1.71 and 1.68 MJ kg^{-1}, respectively (**Supplementary Table 2**), contributing to their evaporation fluxes exceeding the thermodynamic evaporation limit (1.47 kg m^{-2} h^{-1} under 1 sun). This reduced enthalpy is attributed to the presence of intermediate water in SAU and SALi (**Supplementary Fig. 17**). We further evaluate the evaporation performance of the single-stage SAU-based ASP under varying solar fluxes (**Supplementary Fig. 16b**). As the light intensity increases from 0.5 sun to 1.5 sun irradiation, the evaporation flux rises from 0.88 to 2.72 kg m^{-2} h^{-1}. The SALi-based ASP shows comparable evaporation behavior (**Supplementary Table 2**).

2.4 Thermal balance analysis

As the first chamber involves no phase-change heat recovery, the calculation is thus performed on the second chamber to the sixth chamber of the 6-stage ASP. The phase-change heat recovery efficiency (η_{HREi}; i=2, 3, …6) is calculated based on the **Eq. S16** where $\dot{m}_i$ is the evaporation flux of the i^{th} chamber (i=2, 3, …6); h_{lve} is the evaporation enthalpy obtained by DSC measurements, shown in **Supplementary Table 2**; T_{cwi} is the capillary wick's temperature of the i^{th} chamber (i=2, 3, …6); T_0 is the inlet temperature (25 °C); $WPR_{i\text{-}1}$ is the water production rate of the (i-1)th chamber (i=2, 3, …6); $h_{lvc(i\text{-}1)}$ is the condensation latent heat of the (i-1)th chamber (i=2, 3, …6), obtained from the Handbook of Thermodynamics. Note that the inlet water is preheated during operation, providing additional sensible heat that contributes to vapour generation. Given the complexity of the multiple water transfer pathways in the multi-stage ASP the temperature of the bottom water container is adopted as the effective inlet temperature (T_0) for analysis.

$$\eta_{HREi} = \frac{\dot{m}_i \cdot (h_{lve} + C_p(T_{cwi} - T_0))}{WPR_{i\text{-}1} \cdot h_{lvc(i\text{-}1)}} \quad \text{(S16)}$$

The detailed parameters for each stage of ASP are shown below:

i	$\dot{m}_i$ (kg m^{-2} h^{-1})	T_{cwi} (°C)	WPR_i (kg m^{-2} h^{-1})	h_{lvci} (MJ kg^{-1})
1	1.75	42.8	1.26	2.409
2	1.41	38.7	1.01	2.416
3	1.01	35.4	0.76	2.422
4	0.67	32.5	0.51	2.431
5	0.39	29.6	0.30	2.436
6	0.20	27.2	0.15	2.441

Note that $\dot{m}_1$, T_{cw1}, WPR_6, and h_{lvc6} are not used in the phase change heat recovery calculation.

Based on the above parameters and **Eq. S16**, the phase-change heat recovery efficiency (η_{HREi}; i=2, 3, …6) is calculated below:

i	2	3	4	5	6
η_{HREi}	82.3%	72.6%	63.4%	54.7%	47.1%

The phase-change heat recovery efficiency of the ASP declines gradually, mirroring the trend observed in conventional multi-stage systems. In addition, we also compare the temperature of the capillary wick (T_{cwi}) and the condenser (T_{ci}), as below:

i	1	2	3	4	5	6
T_{cwi} (°C)	42.8	38.7	35.4	32.5	29.6	27.2
T_{ci} (°C)	39.1	35.8	32.8	29.8	27.3	26.1

For each chamber, the temperature of the capillary wick is slightly lower than that of the preceding condenser. As a result, a certain amount of heat loss is inevitable during the phase-change heat recovery process, including non-ideal heat release during condensation, conductive heat losses, and other irreversible thermal losses within the enclosed chamber. The primary objective of this calculation is to demonstrate the feasibility and overall trend of multi-stage phase-change heat recovery. Therefore, a strict quantification of the highly coupled heat-transfer processes within the enclosed chamber is not performed. Nevertheless, these heat losses do not alter the fundamental physical mechanism or the main conclusions of this work, namely that the evaporation temperature decreases progressively from chamber to chamber and that a portion of the condensation heat is effectively recovered to drive subsequent evaporation.

Although the multi-stage phase-change heat recovery efficiency has been estimated, the detail energy transfer in the multi-stage system is non-trivial due to the complex inter-stage heat transfer, evaporation-condensation coupling, and distributed heat losses. In particular, the recycled latent heat across stages cannot be clearly represented as independent energy pathways without oversimplification. Therefore, we only evaluate the energy transfer in first chamber of 6-stage ASP under 1 sun. The energy loss is mainly composed of optical loss, radiation loss, convection loss and heat conduction loss. The optical loss (Q_{ol}) is obtained from **Supplementary Fig. 2**. The PV electricity generation (Q_{Eg}) is obtained from **Fig. 3a**. The radiation loss Q_{rad} is calculated by **Eq.**

S17 where A_{eff} is the area of the PV panel; ε is the emissivity; and σ was the Boltzmann's constant (5.67×10^{-8} W m^{-2} K^{-4}); T_{s1} is the steady-state average temperature of the PV panel, and T_{s0} is the ambient temperature (K).

$$Q_{rad} = A_{eff}\varepsilon\sigma(T_{s1}^4 - T_{s0}^4) \quad \text{(S17)}$$

The convective loss Q_{conv} is calculated by **Eq. S18** where h_{eff} is the convective heat transfer coefficien.

$$Q_{conv} = A_{eff}h_{eff}(T_{s1} - T_{s0}) \quad \text{(S18)}$$

The conduction loss Q_{cond} is calculated by **Eq. S19** where C_p is the specific heat capacity of water; m is the mass of water in the bottom tank ; $\triangle T$ was the temperature change of water in the bottom tank within a certain irradiation time.

$$Q_{cond} = C_p m \triangle T \quad \text{(S19)}$$

The energy consumption required for evaporation (Q_{eva}) is calculated by **Eq. S20**.

$$Q_{eva} = 100 - Q_{cond} - Q_{conv} - Q_{rad} - Q_{ol} - Q_{Eg} \quad \text{(S20)}$$

Based on the above Equations, a Sankey diagram can be obtained in **Supplementary Fig. 18**.

2.5 Outdoor experiments

The outdoor experiments are conducted in Shenzhen (China). The experiment is conducted in natural seawater (from the South China Sea). The weather conditions are recorded by the weather station (FT-SQ5, China; TES-1333R, China). The PV output is recorded by PV meter (PVT801, China). The condensed water is collected every 2 hours to calculate the outdoor water production rate. The sum of the water production rate is water production amount. The related weather conditions and water production performance for each time period are as follows:

Time period	Average solar flux (kW m^{-2})	Average wind speed (m s^{-1})	Average WPR (kg m^{-2} h^{-1})	PV temperature (°C)
08:00-10:00	0.48	1.09	1.93	27.8
10:00-12:00	0.71	2.44	2.55	40.1
12:00-14:00	0.72	2.08	2.59	40.6
14:00-16:00	0.51	1.40	2.11	36.1
16:00-18:00	0.17	0.82	0.81	28.1

The ion concentrations in the corresponding condensed water, the original seawater, and the concentrated seawater are measured by ICP-OES. Before calculating the adsorption capacity (*AC*), the solution in the tank is replenished to its original weight with deionized water. The adsorption capacity (*AC*) is still calculated using **Eq. 3**, where C_0 and C_e are provided in **Supplementary Tables 5** and **6**; V is 40 L, and S is 1920 cm^2. The ion recovery efficiency (IRE) is calculated according to **Eq. S21**, *ca* 83.2% for lithium and 90.1% for uranium, respectively.

$$IRE = \frac{AC \cdot S}{V \cdot C_0} \tag{S21}$$

The ASP's selectivity for lithium and uranium ion under the competing cations of seawater is analyzed by using the selectivity coefficient, which can be calculated by **Eqs. S22** and **S23**[74].

$$\alpha_{Me}^{Li} = \frac{q_{e\text{-}Li}/C_{e\text{-}Li}}{q_{e\text{-}Me}/C_{e\text{-}Me}} \quad \text{(S22)}$$

$$\alpha_{Me}^{U} = \frac{q_{e\text{-}U}/C_{e\text{-}U}}{q_{e\text{-}Me}/C_{e\text{-}Me}} \quad \text{(S23)}$$

Where α_{Me}^{Li} and α_{Me}^{U} are the selectivity coefficient of lithium ion and uranium ion to other metal ions, respectively; $q_{e\text{-}Li}$ and $q_{e\text{-}U}$ are the lithium and uranium adsorption capacity in seawater, respectively; $C_{e\text{-}Li}$ and $C_{e\text{-}U}$ are the lithium ion and uranium ion concentration after outdoor experiments, respectively; $q_{e\text{-}Me}$ is the adsorption capacity of other metal ions in seawater; $C_{e\text{-}Me}$ is the ion concentration of other metal ions after outdoor experiments. All above parameters are provided in **Supplementary Tables 5** and **6.**

2.6 Technology and economic analysis

(1) The annual output estimation of ASP

The ASP's output is calculated below: The average solar flux of the outdoor experiment is about 0.52 sun, and the outdoor operation time is about 10 h. Based on this outdoor data and the average daily solar flux in Hong Kong (~ 5.2 kWh m^{-2}), the annual ASP output can be estimated below:

Outdoor experiments	Total solar flux: 5.2 kW h m^{-2}	PV output (kW h m^{-2})	WPR (kg m^{-2})
		1.02	19.82
		Uranium (mg m^{-2})	Lithium (mg m^{-2})
		0.71	31.23
Estimated annual ASP output	Total solar flux: 1460 kW h m^{-2}	PV output (kW h m^{-2})	WPR (kg m^{-2})
		286	5570
		Uranium (g m^{-2})	Lithium (g m^{-2})
		0.20	8.77

In view that LiCl and $UO_2CO_3 \cdot Na_2CO_3$ are the typical high-value chemical products for the lithium and uranium industries, the products of the ASP can be converted into industrial products of equivalent value based on the principle of conservation of elements. The annual ASP output can be estimated below:

Items	Output	Items	Output
PV output (kW h)	286	Electricity (kW h)	286
WPR (kg)	5570	Clean water (kg)	5570
Uranium ion (g)	0.20	$UO_2CO_3 \cdot Na_2CO_3$ (g)	0.403
Lithium ion (g)	8.77	LiCl (g)	53.5

The annual ASP output can be estimated below. Note: The price of the electricity, water, $UO_2CO_3 \cdot Na_2CO_3$ and LiCl come from https://www.globalpetrolprices.com/China/electricity_prices/ https://www.energymonitor.ai/tech/can-desalination-save-a-drying-world/,

https://www.cameco.com/invest/markets/uranium-price and https://www.cbcie.com/lithium/price/list/600593.html, respectively. The area of ASP is about 1 m^2:

Items	Output	Items	Profit (US$)
Electricity (kW h)	286	Electricity	20.03
Clean water (kg)	5570	Clean water	5.56
$UO_2CO_3 \cdot Na_2CO_3$ (g)	0.403	$UO_2CO_3 \cdot Na_2CO_3$	0.065
LiCl (g)	53.5	LiCl	0.54
Total	-	Total	26.20 US$

(2) The extraction cost analysis

From a complete life-cycle perspective, the total cost of seawater resource extraction by ASP can be divided into fabrication, operating, maintenance and decommissioning cost.

■ The fabrication cost of ASP

The costs of each unit when fabricating 1 m^2 6-stage ASP (the first three stages are SAU and the last three are SALi) are listed below:

Item	Value	Amount	Sum (US$)
PV panel	~ US$ 42.1 m^{-2}	1 m^2	42.1
Waterproof glue	~ US$ 4.02 L^{-1}	0.5 L	2.01
Aluminum tape	~ US$ 2.1 m^{-2}	6 m^2	12.6
Acrylic frame	~ US$ 10.2 m^{-2}	1.2 m^2	12.24
Bolt	~ US$ 0.14 $item^{-1}$	12 items	1.7
Condensation plate	~ US$ 4.2 m^{-2}	1 m^2	4.2
Human resource	~ US$ 3.7 m^{-2}	1 m^2	3.7
Total			US$ 78.55

Assuming the capillary wick (SAU and SALi) is replaced annually (see below), the capillary wick related costs are included in the maintenance and operating cost.

■ The operation and maintenance cost of the ASP

Since the ASP operates under natural solar irradiation, its operating costs mainly come from seawater pumping cost and capillary regeneration cost (including displacement and crystallization cost). Given the saturated adsorption capacity of SAU and SALi, SAU and SALi in the ASP needs to be regenerated every ~1/3 year and > 3 years, respectively. SALi is regenerated by hydrochloric acid solution, and the resulting solution is evaporated and crystallized to obtain pure LiCl. The cost of displacement and crystallization is approximately US$ 1.68 kg^{-1} LiCl. SAU is regenerated using sodium carbonate solution, and the resulting solution is desorbed, impurity-removed, evaporated and crystallized to obtain $UO_2CO_3 \cdot Na_2CO_3$. The related cost is approximately US$ 1.79 kg^{-1} $UO_2CO_3 \cdot Na_2CO_3$. Based on the ASP output, the cost of the regeneration process is shown below (Note: The area of ASP is about 1 m^2):

Items	**Output (g)**	**Items**	**Cost**
$UO_2CO_3 \cdot Na_2CO_3$	0.403	$UO_2CO_3 \cdot Na_2CO_3$	0.72×10^{-3}
LiCl	53.5	LiCl	9.01×10^{-2}
Total	-	Total	US$ 9.08×10^{-2}

We assume that the capillary wick is replaced annually. Rather than recycling the adsorbent from the capillary wick, the wick is incinerated, which leads to negligible disposal costs. The capillary wick-related costs are shown below.

Item	**Value**	**Amount**	**Sum (US$)**
SAU	~ US$ 1.4 m^{-2}	3 m^2	4.2
SALi	~ US$ 3.4 m^{-2}	3 m^2	10.2
Non-woven fabrics	~ US$ 0.2 m^{-2}	12 m^2	2.4
Total			US$ 16.8

The seawater pumping cost is estimated as follows: In the one-day outdoor experiment, the PV panel of ASP has an area of 0.192 m^2, and the corresponding ASP water tank volume is 57.6 L. Under the same operating conditions, the annual seawater pumping

volume for a 1 m^2 ASP can be obtained. The used pump has a pump efficiency of 50%, and an electricity price of approximately US$ 0.10 kWh^{-1}, thus resulting in an estimated energy consumption of approximately 0.02 kWh m^{-3} seawater. Based on these, the annual pumping energy consumption and associated cost for a 1 m^2 ASP can be calculated below.

Project	Value	Project	Value
Daily seawater pumping amount	300 L	Annual pumping energy consumption	2.2 kWh
Annual seawater pumping amount	110 m^3	Annual pumping cost	US$ 0.20

Because the ASP is essentially a type of PV system, its maintenance cost can be estimated following standard PV TEA methodology. Typically, annual maintenance costs account for approximately 1% of the initial capital investment (~ US$ 1.02)[75]. Overall, the annual operation and maintenance cost of the 1 m^2 ASP is approximately US$ 18.11.

■ The decommissioning cost of ASP

Since the ASP is essentially a type of PV system, its decommissioning cost can be estimated following standard PV TEA methodology. Typically, the decommissioning costs are negligible[76], as materials such as aluminum from the dismantled PV panels can be recycled.

■ The total annual extraction cost of ASP

Before calculation, we assume that the service life of ASP is 20 years. The total annual extraction cost of ASP can be calculated based on **Eq. S24** where C_{aec}, C_{fc}, C_{omc}, and C_{dc} are the total annual extraction cost, fabrication cost, operating and maintenance cost, and decommissioning cost, respectively.

$$C_{aec} = \frac{C_{fc} + C_{omc} \times 20 + C_{dc}}{20} \quad \text{(S24)}$$

Given that the ASP can produce various products, including electricity, water, lithium, and uranium, the extraction cost of these products is calculated using the product profit

allocation method based on **Eq. S25** where $C_{aec\text{-}i}$ is the extraction cost of different products (i=electricity, water, lithium, and uranium), $C_{pp\text{-}i}$ is the product annual profit (i=electricity, water, lithium, and uranium), and C_{pp} is the product annual profit.

$$C_{aec\text{-}i} = \frac{C_{pp\text{-}i}}{C_{pp}} C_{aec} \tag{S25}$$

The extraction cost of various product is shown in **Supplementary Table 7**.

(3) Sensitivity analysis of annual net income

The annual net income over the entire service life (assumed as 20 years here) is influenced by the lifespan of the capillary wicks. Therefore, a sensitivity analysis of the ASP is performed on the annual net income under different lifespan of the capillary wicks based on **Eq. S26** where C_{ani} is the annual net income; C_{rc} and C_{mc} are the regeneration cost and maintenance cost, respectively (the sum of C_{rc} and C_{mc} are US$ 1.31); C_{ccw} is the cost of capillary wicks (US$ 16.8); N is the lifespan of capillary wicks (1, 2, 3,… and 20).

$$C_{ani} = \frac{C_{pp} \times 20 - C_{fc} - (C_{rc} + C_{mc}) \times 20 - \frac{20}{N} \times C_{ccw}}{20} \tag{S26}$$

2.7 Environmental impact analysis of ASP based on a cradle-to-grave life cycle assessment (LCA)

(1) Objectives, scope, and system boundary

This study conducts a LCA to quantify the environmental impacts associated with ASP, primarily including the following indexes: Global Warming Potential, Primary Energy Demand, Water Consumption, Eutrophication Potential, and Human Toxicity Potential, etc. The LCA methods follow ISO 14040 and ISO 14044 standards[77, 78]. The functional unit is defined as the treatment of 1 m^3 of seawater using the ASP. All environmental impact indicators are normalized to this functional unit to ensure comparability and consistency. The system boundary contains three main stages: (i) ASP fabrication, including PV panel manufacturing, capillary wick fabrication, and the production of external frames and connectors; (ii) operation and maintenance, such as capillary wick regeneration and replacement, as well as pumping processes; and (iii) decommissioning, including the recovery of high-value components and the disposal of non-recyclable materials. Infrastructure construction, transportation, capital equipment, and human resources are excluded from the assessment, consistent with laboratory-scale LCA practices and not expected to change comparative conclusions. The service life of the ASP is assumed to be 20 years, while the capillary wicks (SAU and SALi) are replaced annually.

(2) Life cycle inventory

■ The fabrication inventory

The abbreviations of "Global Warming Potential, Primary Energy Demand, Water Consumption, Eutrophication Potential, and Human Toxicity Potential" is GWP, PED, WC, EP, and HTP, respectively, with the unit of "kg CO_2-eq $unit^{-1}$, MJ $unit^{-1}$, L $unit^{-1}$, kg PO_4-eq $unit^{-1}$, kg 1,4-DCB-eq $unit^{-1}$". The emission factors used in the fabrication section are shown below (Note: (1) The most used data come from the Ecoinvent v3.8 database; (2) Aluminum materials assume secondary aluminum production):

Component	Unit	GWP	PED	WC	EP	HTP
PV module	m^2	900	12000	2000	0.5	150
Aluminum tape	kg	2.5	20	10	2.0×10^{-3}	0.5
Acrylic frame	kg	3.8	90	30	4.0×10^{-3}	1.1
Steel (bolt)	kg	2.1	35	15	2.5×10^{-3}	0.6
Waterproof glue	kg	3.2	80	25	3.5×10^{-3}	0.9
Condensation plate	kg	8.6	150	80	1.0×10^{-2}	2.4

■ The regeneration and operation inventory:

Emission factors used in this section are shown below:

Component	Unit	GWP	PED	WC	EP	HTP
Electricity (China grid)	kW h	0.7	8.5	2	1.8×10^{-4}	0.12
HCl (Industrial)	kg	1.6	12	15	3.0×10^{-3}	0.45
Na_2CO_3 (Solvay process)	kg	1	8	10	2.0×10^{-3}	0.35
Fresh water (Process)	m^3	0.35	5	1000	8.0×10^{-5}	0.05

■ The capillary wick replacement inventory (annual):

Emission factors used in this section are shown below (the disposal emission of the capillary wick is included inside):

Component	Unit	GWP	PED	WC	EP	HTP
SAU + non-woven fabrics	m^2	3.9	82.5	60	6.25×10^{-3}	1.275
SALi + non-woven fabrics	m^2	4.3	87.5	65	7.25×10^{-3}	1.425

■ The decommissioning inventory:

The decommissioning impacts of the ASP mainly arise from the treatment of PV

modules and structural metallic components, particularly aluminum. Aluminum components are assumed to be recycled at high recovery rates (>95%), consistent with industrial practice for construction-grade aluminum. Therefore, aluminum-related decommissioning emissions are substantially reduced but not assumed to be zero. For a typical PV system, the decommissioning stage typically contributes approximately less than 10% of total cradle-to-grave emissions[79], with the majority of impacts occurring during PV manufacturing stages.

(3) Environmental indicators

Based on the above parameters, the detailed environmental indicators can be obtained, as shown below:

Environmental indicators	Value per m^3
GWP	15.4 kg CO_2-eq
PED	195 MJ
WC	470 L
EP	1.9×10^{-2} kg PO_4-eq
HTP	5.3 kg 1,4-DCB-eq

Based on the profit margin of each product, the total emissions are allocated to each product, with the results shown in **Supplementary Table 8**. Given that ASP enables the co-production of four products, that is, electricity, freshwater, lithium salts, and uranium compounds, we have benchmarked their environmental impacts against established industry technologies, namely PV (~49.9 g CO_2-eq per kW h)[80], seawater reverse osmosis (~3.258 kg CO_2-eq per m^3)[81], brine-based lithium extraction (~17.4 kg CO_2-eq per kg)[82], and conventional uranium processing systems (~52 kg CO_2-eq per kg)[81]. The comparison results are shown in **Fig. 5i**. Note that while additional environmental indicators (e.g., PED, WC, EP, and HTP) are also relevant, GWP is selected for benchmarking because it is the most consistently reported metric across LCA studies of the above systems, thereby ensuring comparability.

(4) Sensitivity analysis

To evaluate the influence of capillary wick lifespan on the overall environmental performance of the ASP, a one-factor sensitivity analysis is conducted, taking GWP as an example. In this sensitivity analysis, the total GWP values are calculated by varying the capillary wick lifespan from 1 to 20 years while keeping all other parameters constant. The results are shown in **Fig. 5j**.

3 Supplementary Figures and Tables

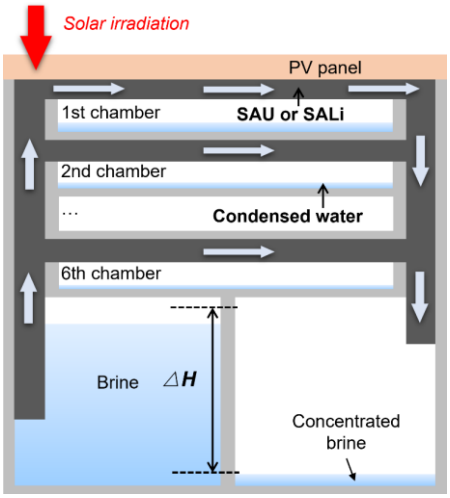

Supplementary Fig. 1 | The schematic diagram of ASP.

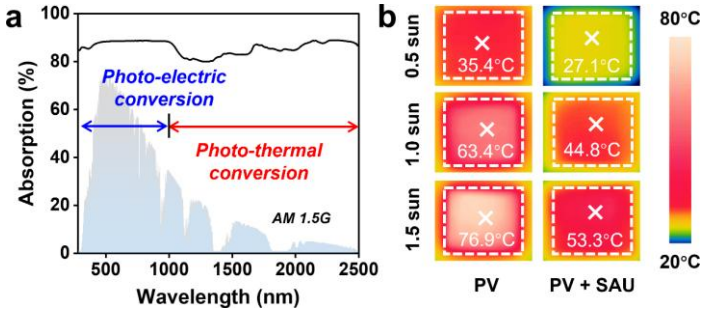

Supplementary Fig. 2 | Photothermal conversion ability of commercial PV panel. (a) UV-Vis-NIR spectra of commercial PV panel; and (b) Infrared photos of PV panel with or without SAU under different solar flux.

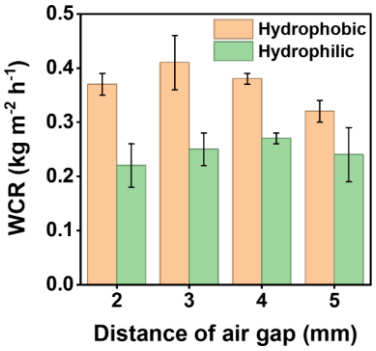

Supplementary Fig. 3 | The water collection rate (WCR) of the aluminum foil with different wettability and air gap distance (Data are presented as mean values ± standard deviation from three independent experiments).

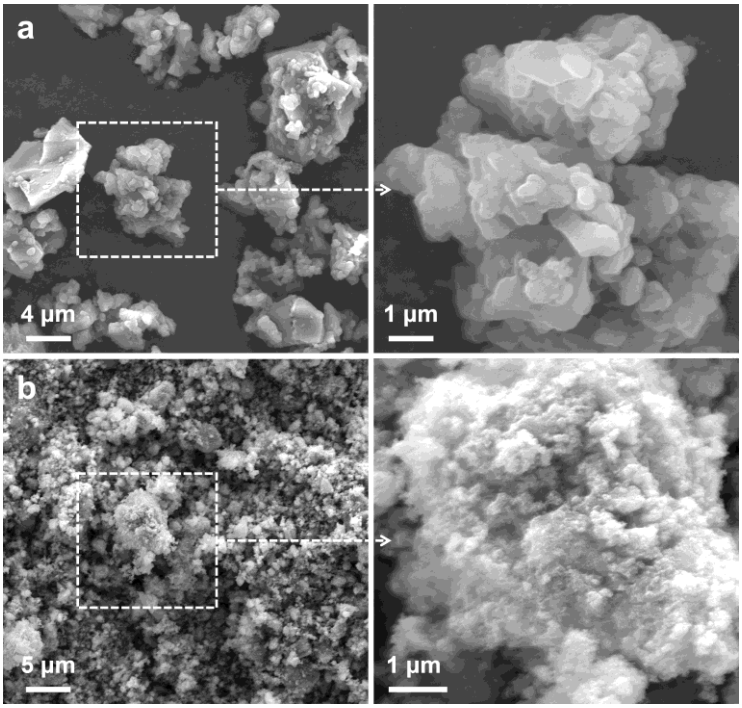

Supplementary Fig. 4 | SEM images: (a) PPC; and (b) HMO.

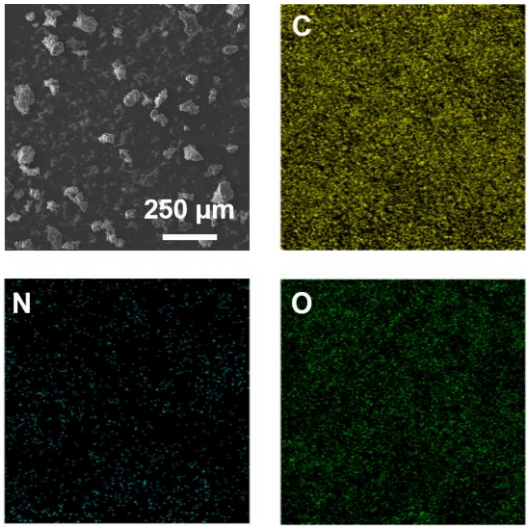

Supplementary Fig. 5 | EDS mapping images of PPC.

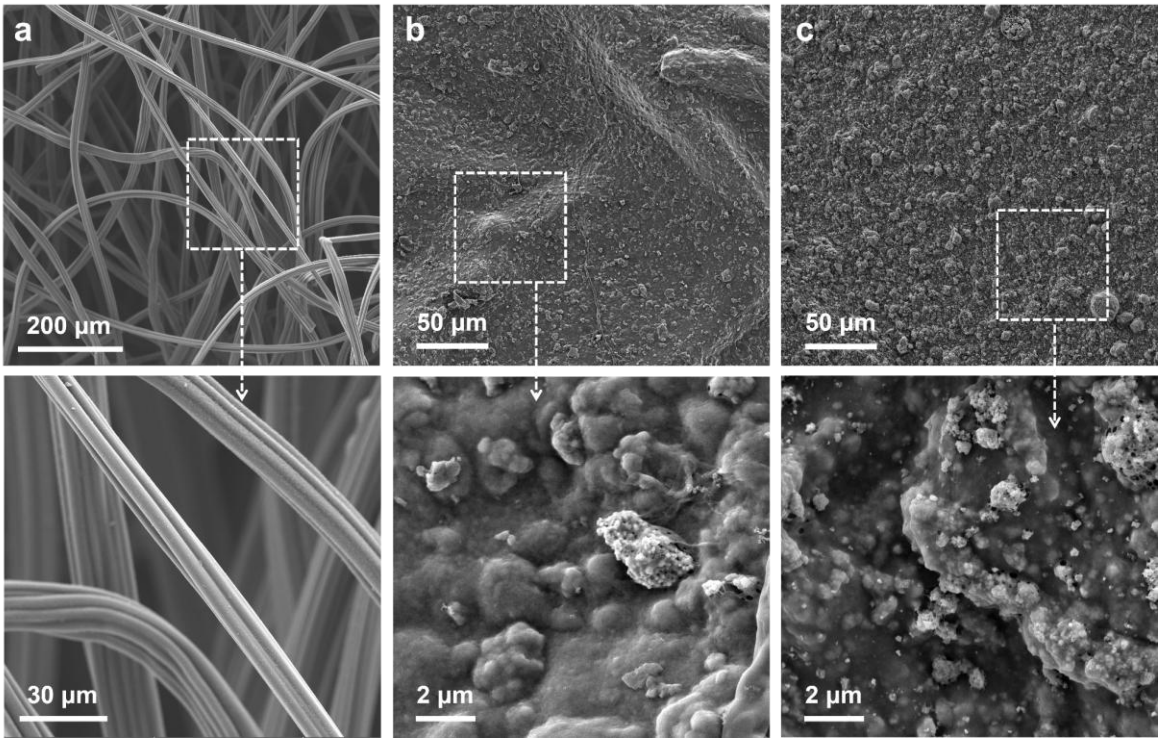

Supplementary Fig. 6 | SEM images: (a) carbon felt; (b) SAU; and (c) SALi.

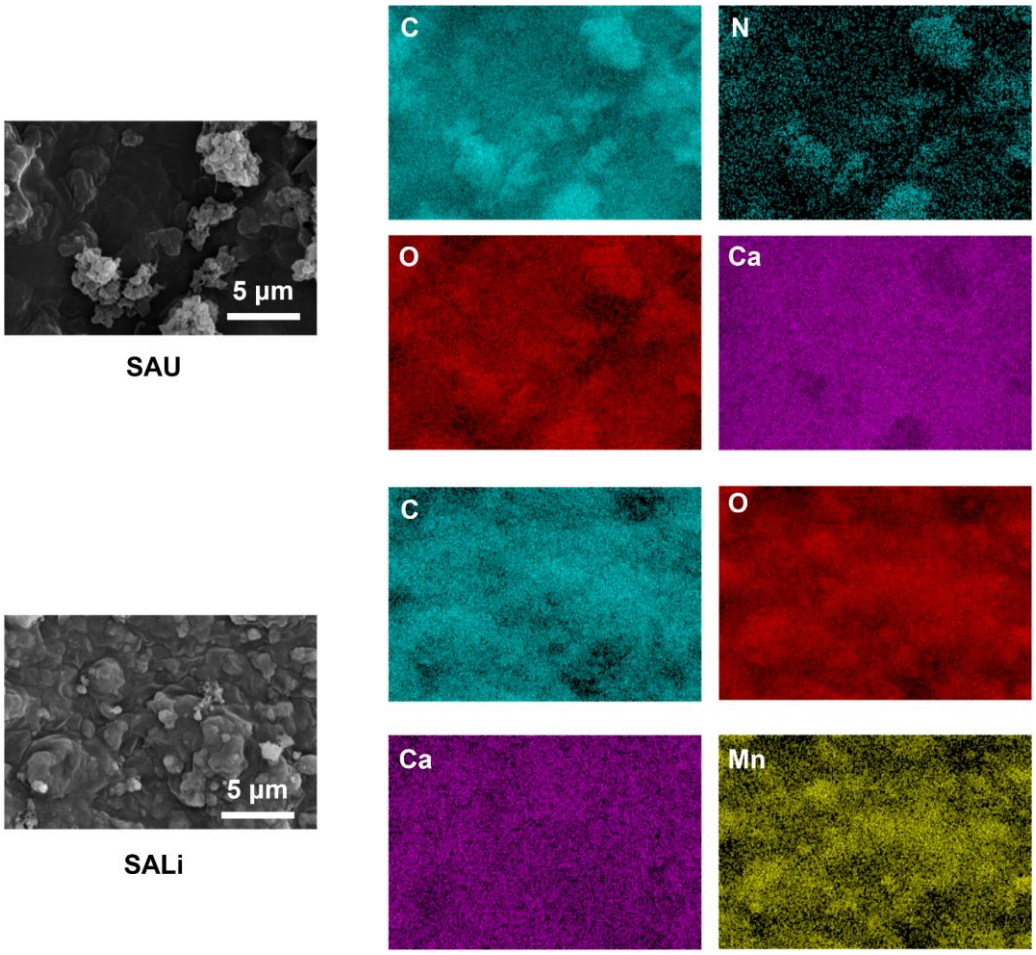

Supplementary Fig. 7 | EDS mapping images of SAU and SALi.

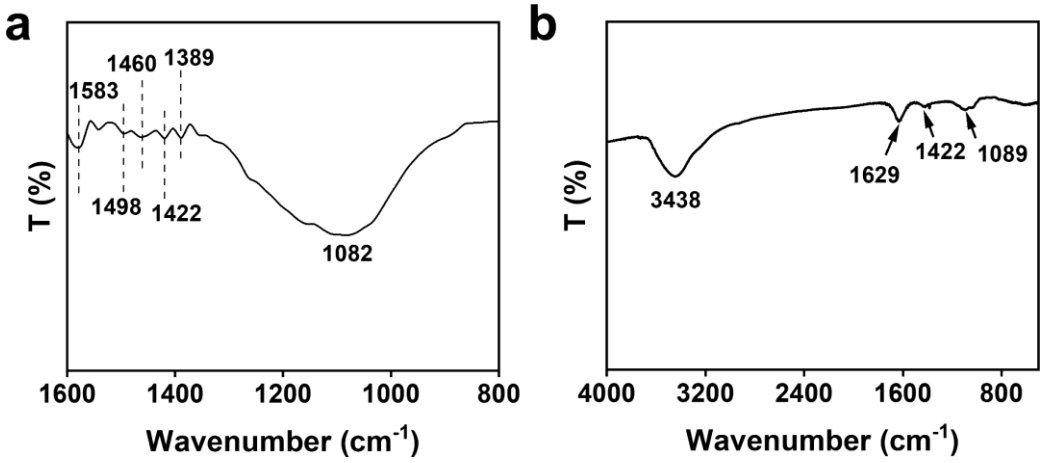

Supplementary Fig. 8 | FTIR spectra: (a) PPC; and (b) SAU

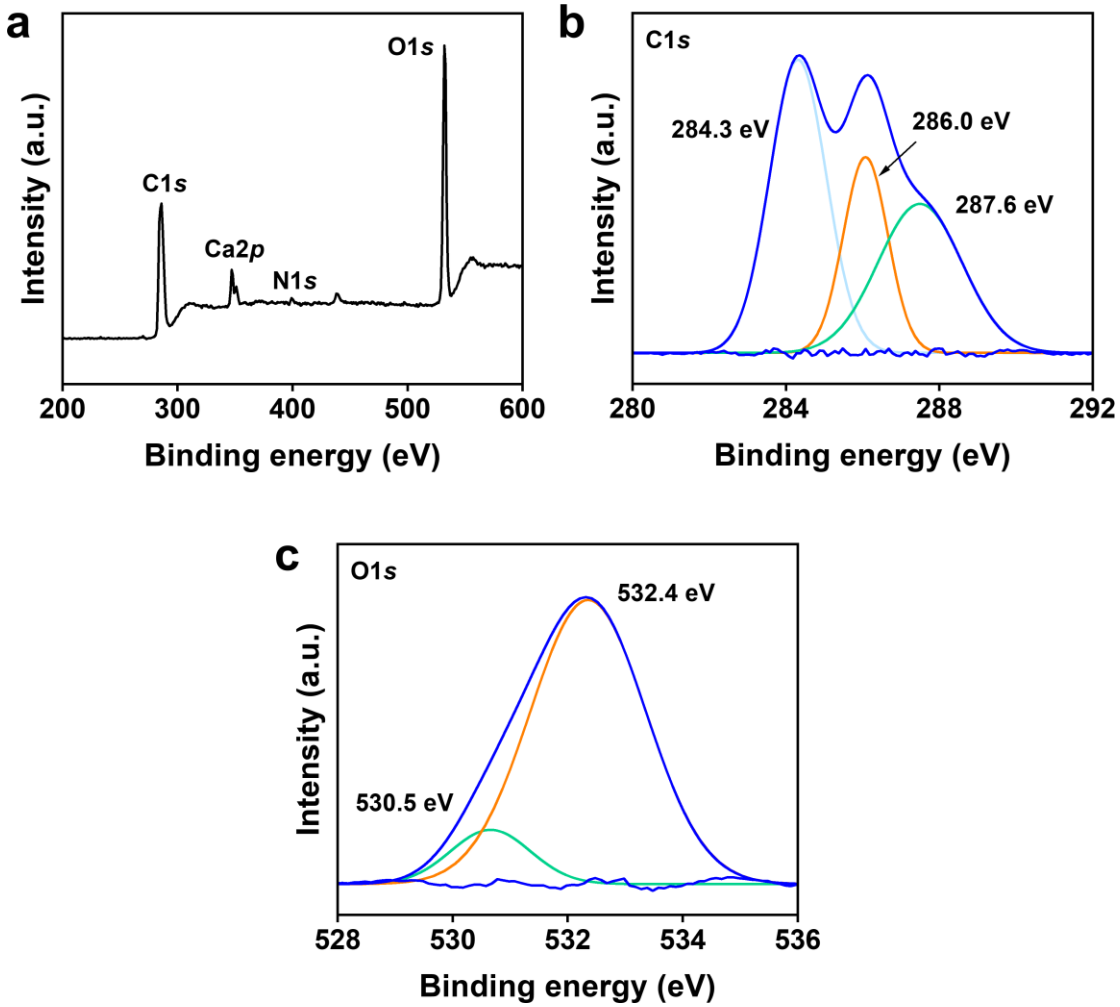

Supplementary Fig. 9 | XPS spectra of SAU: (a) Full survey spectrum; (b) The high-resolution C1*s*; and (c) The high-resolution O1*s*.

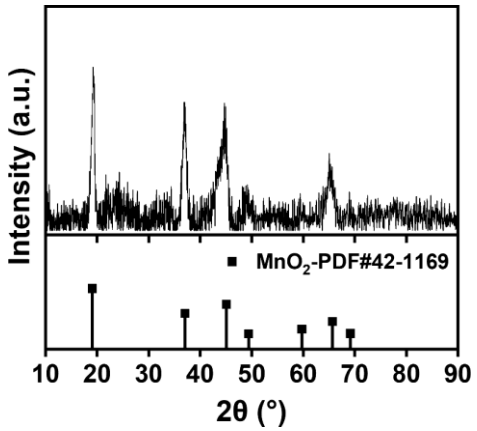

Supplementary Fig. 10 | XRD patterns of SALi.

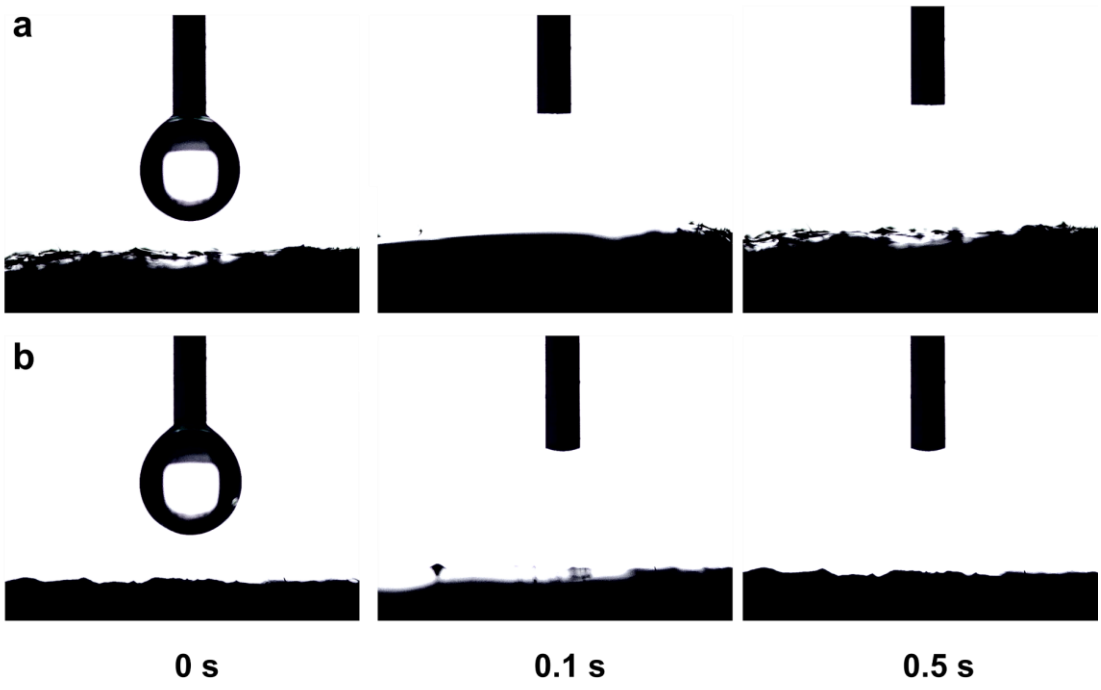

Supplementary Fig. 11 | Water contact angle of (a) SAU; and (b) SALi.

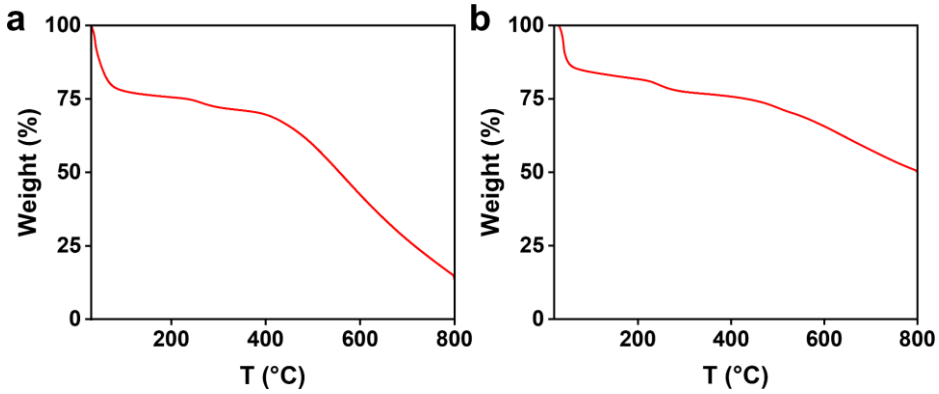

Supplementary Fig. 12 | Thermogravimetric curves: (a) SAU; and (b) SALi.

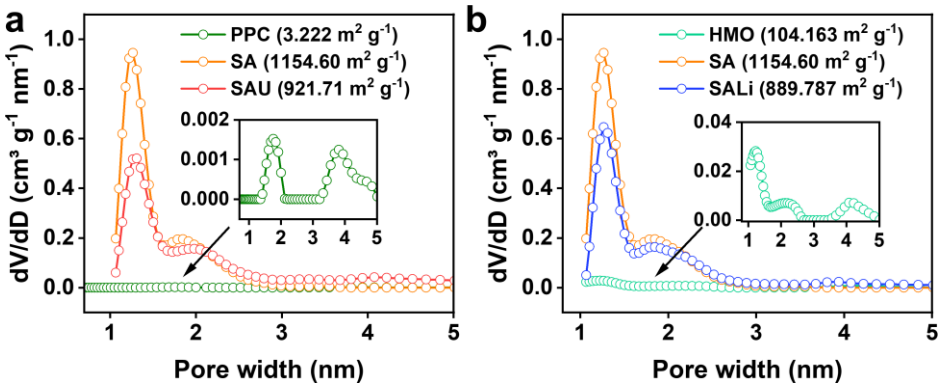

Supplementary Fig. 13 | Pore size distribution of (a) PPC, SA, and SAU; and (b) HMO, SA, and SALi.

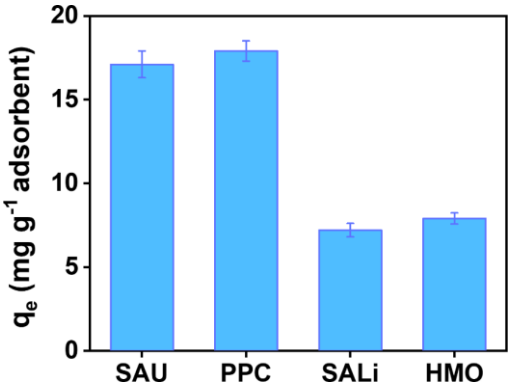

Supplementary Fig. 14 | Adsorption capacity based on adsorbent (Data are presented as mean values ± standard deviation from three independent experiments). Compared to pristine powder adsorbents (PPC and HMO), the adsorption capacity of SAU and SALi reduces ~4.5% and 8.9%, respectively. The adsorption experiments are conducted in 2.5 mg L^{-1} uranium solution or 2.5 mg L^{-1} lithium solution.

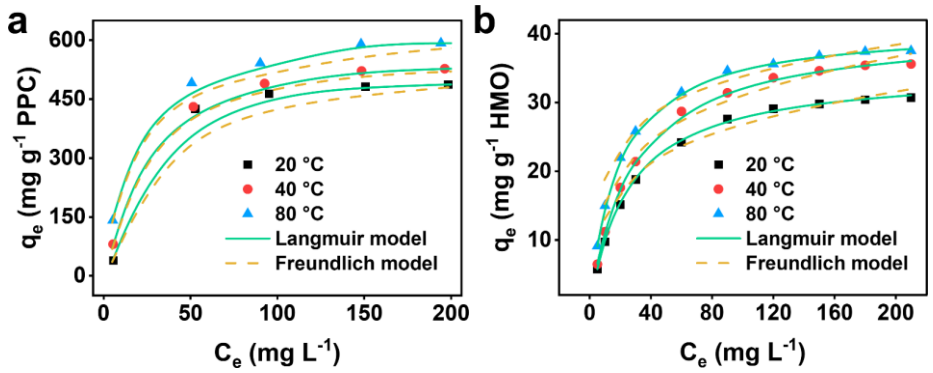

Supplementary Fig. 15 | The adsorption isotherms: (a) SAU; (b) SALi.

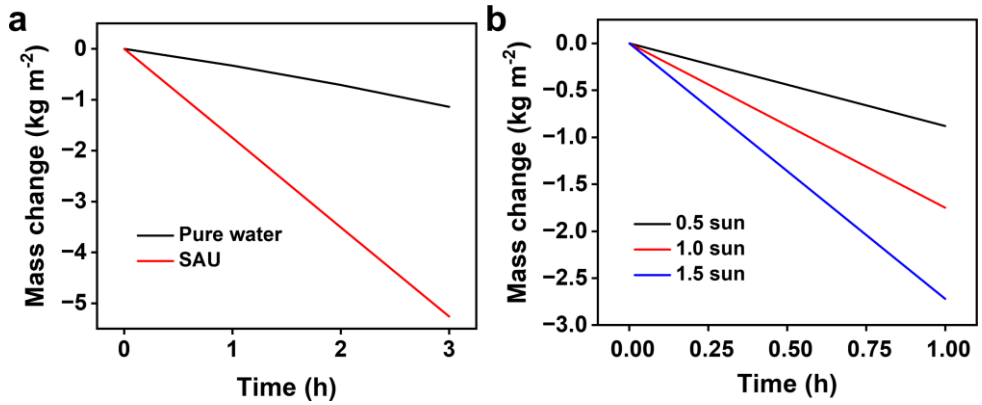

Supplementary Fig. 16 | (a) Mass change curves of SAU-based single-stage ASP and pure water under 1 sun; and (b) Mass change curves of SAU-based single-stage ASP under different solar flux.

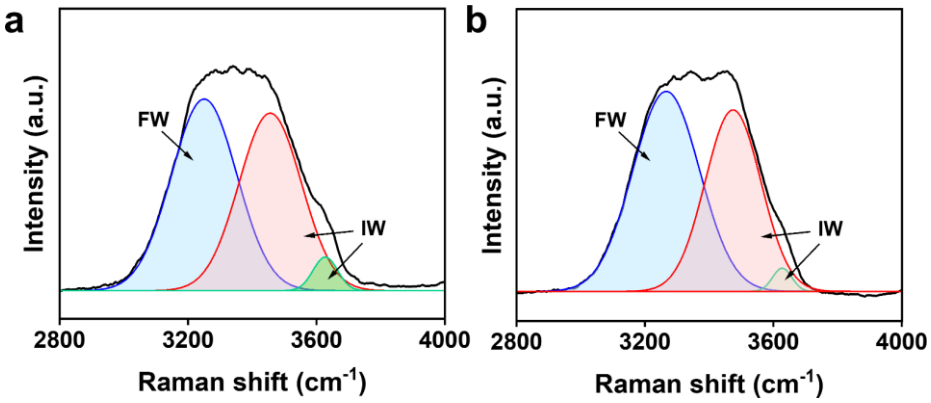

Supplementary Fig. 17 | Raman curves of water in (a) SAU; and (b) SALi.

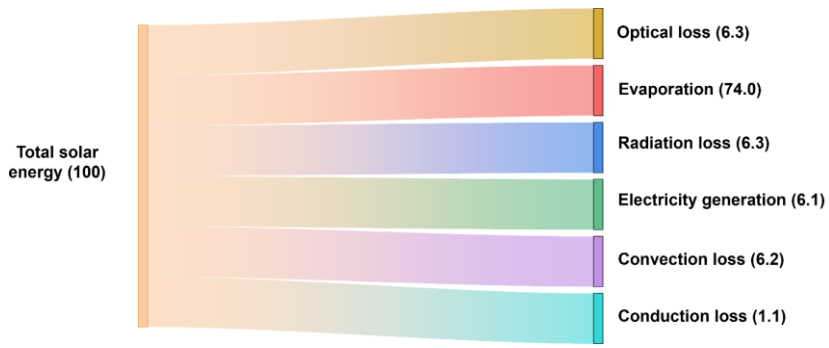

Supplementary Fig. 18 | Sankey diagram of the energy transfer in the first chamber of the 6-stage ASP under 1 sun.

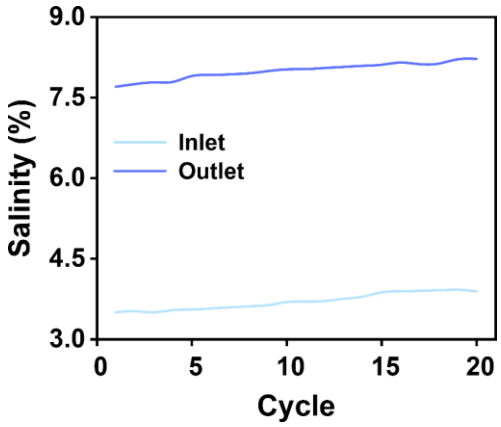

Supplementary Fig. 19 | The outlet and inlet salinity of the capillary wick in the first chamber of the 6-stage ASP during the cycle experiments. The outlet and inlet salinity is recorded by a salinity meter (ADSTR-501, ADVA Lab, USA). The wick in the first chamber exhibits the highest evaporation flux, resulting in the highest outlet salinity. As saturation is not reached in the wick of the first chamber, all subsequent chambers of the 6-stage remain below saturation.

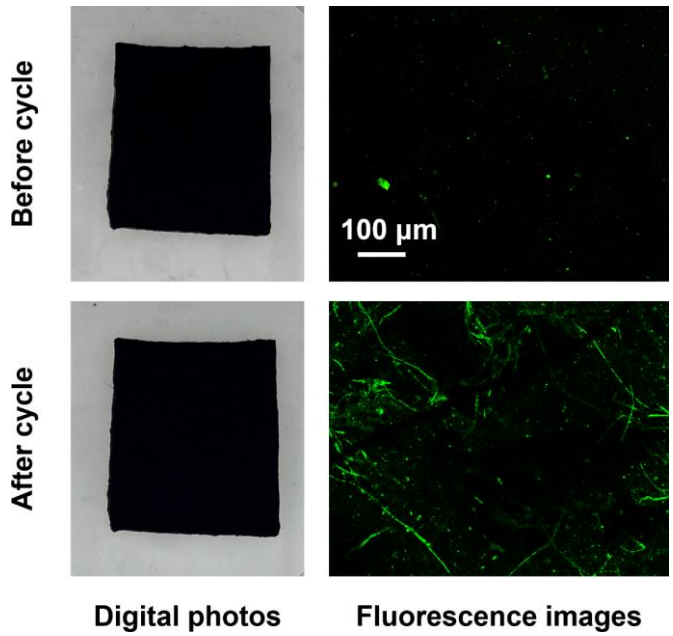

Supplementary Fig. 20 | Digital photographs and partial three-dimensional fluorescence images of the SAU before and after cyclic experiments. Live-cell staining is performed using SYTO 9 Green Fluorescent Nucleic Acid Stain (SYTO9). Samples are incubated with SYTO9 at a final concentration of 5 μM at room temperature for 30 min in the dark. After staining, samples are mounted on glass slides and imaged using a laser scanning confocal microscope. SYTO9 fluorescence is excited at 488 nm and detected between 500 and 550 nm. Green fluorescence indicates living cells. Even after cyclic experiments, no noticeable salt deposition or biofilm formation is observed on the surface of the capillary wick. Although the seawater and capillary wick are not sterilized, only a sparse microbial presence is detected on the wick surface under long-term operating conditions. Importantly, the high-salinity environment of the capillary wick effectively suppresses microbial proliferation, thereby preventing the formation of a thick and continuous biofilm.

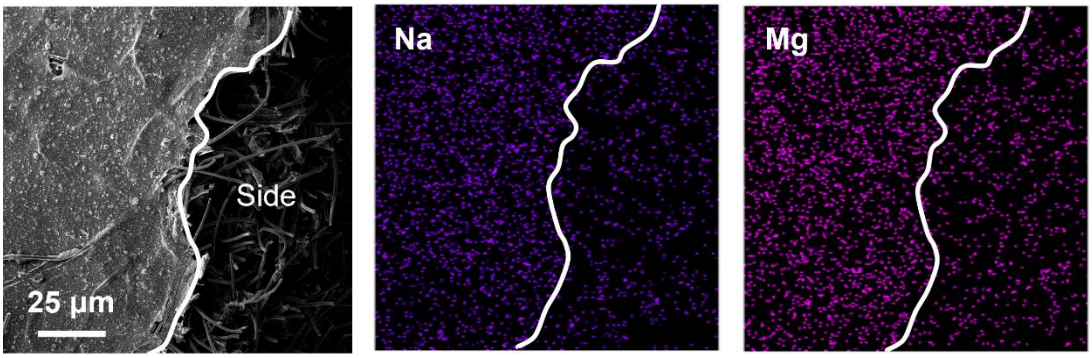

Supplementary Fig. 21 | EDS mapping images of SAU after the cycle experiment. After the cycling experiments, the unwashed SAU samples are directly dried and subjected to EDS analysis, representing a worst-case scenario for potential salt accumulation. Considering that SAU is crosslinked by Ca^{2+} and that Ca^{2+}, Na^{+}, Mg^{2+}, and K^{+} are the major ions present in seawater, the elemental analysis focused on Na^{+}, Mg^{2+}, and K^{+}. The results show that the potassium (K) signal is below the detection limit, and therefore, no corresponding elemental mapping is presented. The atomic contents of magnesium (Mg) and sodium (Na) are relatively low, at 0.66% and 1.88%, respectively. In addition, SEM observations revealed no obvious large salt crystallization from the side part of SAU. These observations indicate that no significant macroscopic salt accumulation or surface pore blockage occurs on SAU after repeated cycling. Combined with the stable adsorption performance over multiple cycles, the results suggest that pore clogging does not occur.

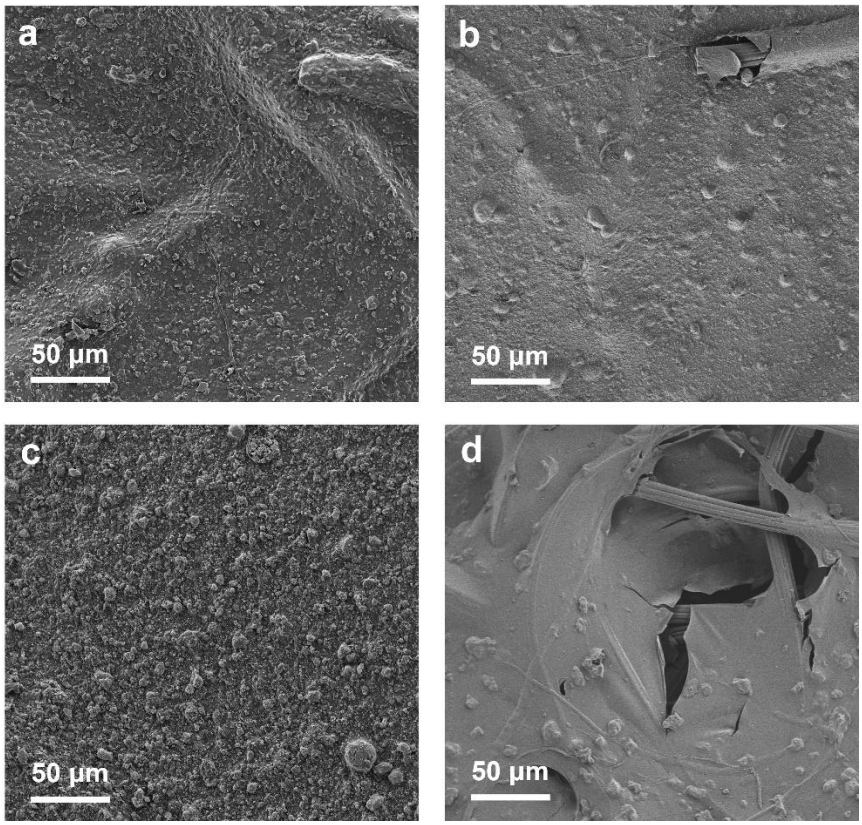

Supplementary Fig. 22 | SEM images of SAU: (a) before and (b) after cyclic experiments. SEM images of SALi: (c) before and (d) after cyclic experiments. After cyclic experiments, the surface of the capillary wicks (SAU and SALi) became smooth.

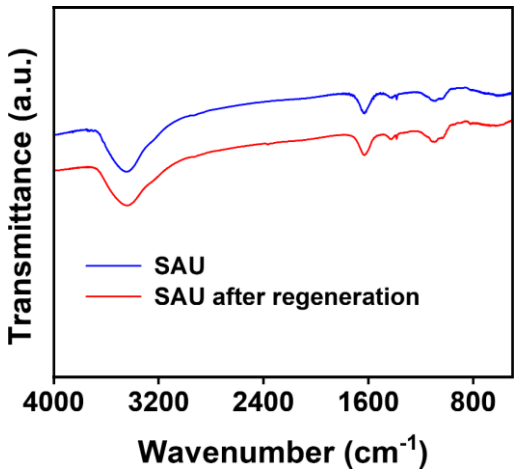

Supplementary Fig. 23 | FTIR spectra of SAU before and after regeneration.

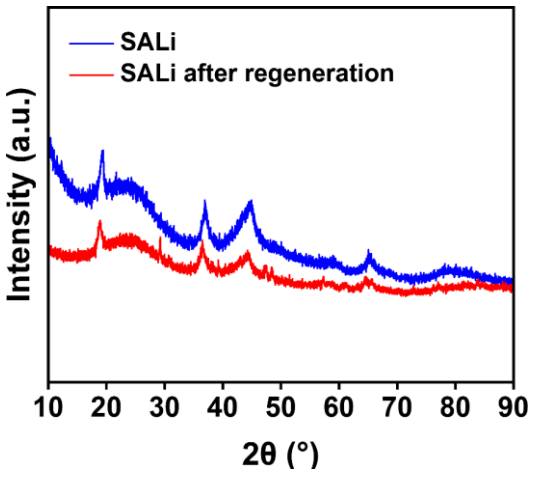

Supplementary Fig. 24 | XRD patterns of SALi before and after regeneration.

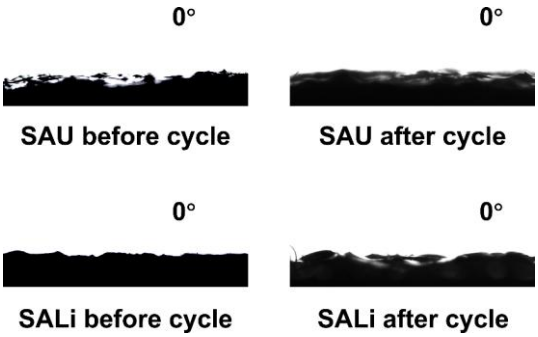

Supplementary Fig. 25 | The water contact angle of different samples. SAU and SALi still exhibit hydrophilicity after cycle experiment because their water contact angle remained ~ 0°.

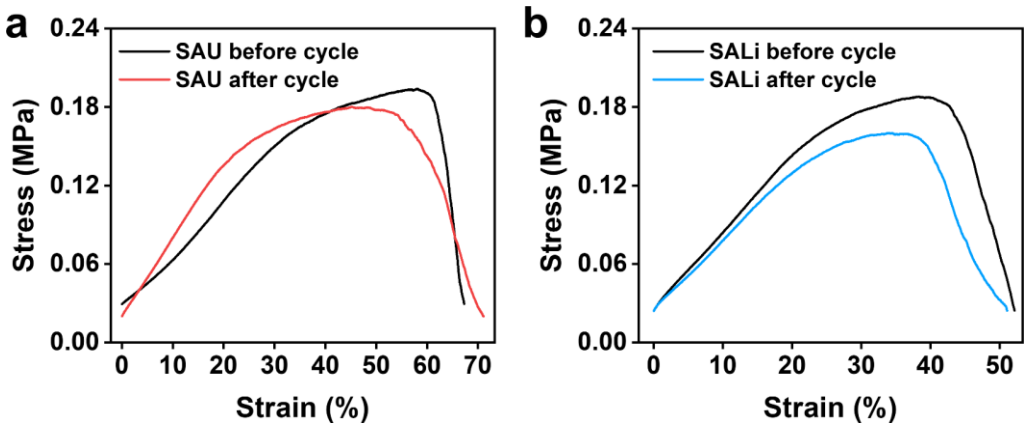

Supplementary Fig. 26 | Tensile stress-strain curves: (a) SAU before and after cyclic experiments and (b) SALi before and after cyclic experiments. From these curves, the tensile strength of SAU shows little change (0.19 MPa before vs. 0.18 MPa after cycling), while that of SALi decreases by about 13% (from 0.19 MPa to 0.16 MPa). Correspondingly, the mass losses after cycling are 3.7% for SAU and 5.5% for SALi. Overall, both SAU and SALi exhibit good mechanical performance and mass integrity after repeated cycling, with SAU exhibiting slightly better stability.

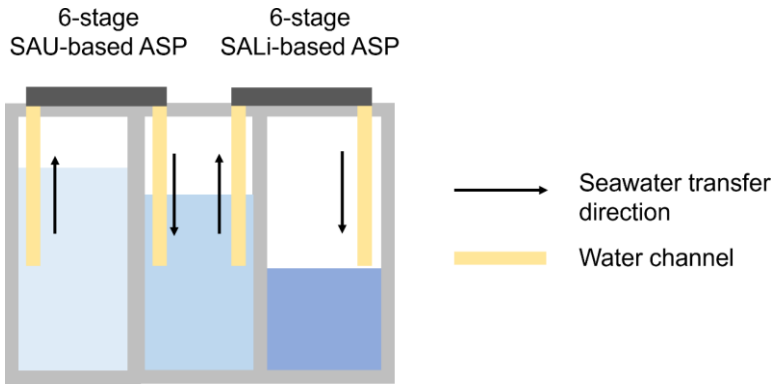

Supplementary Fig. 27 | Structural diagram of the series connection of 6-stage SAU-based ASP and SALi-based ASP.

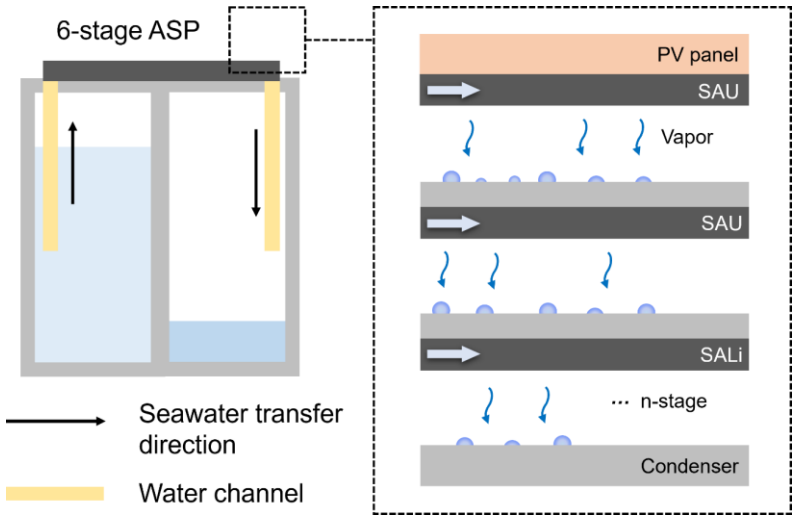

Supplementary Fig. 28 | Structural diagram of the parallel combination of SAU and SALi in a single six-stage ASP.

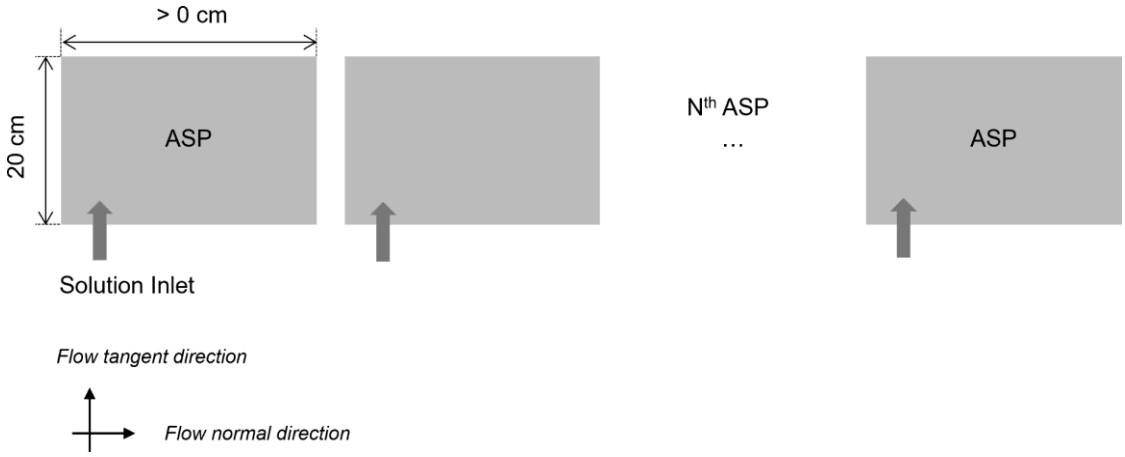

Supplementary Fig. 29 | Diagram of the ASP scaling way when large-area implementation. Note that every ASP has its own solution inlet.

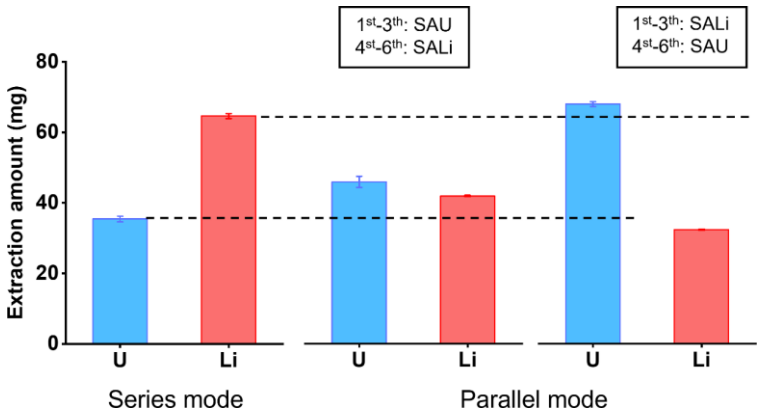

Supplementary Fig. 30 | The uranium ion (U) and lithium ion (Li) extraction amounts by ASP under different modes (Data are presented as mean values ± standard deviation from three independent experiments). The extraction experiments are conducted in real seawater spiked with 2.5 mg L^{-1} uranium ion and 2.5 mg L^{-1} lithium ion.

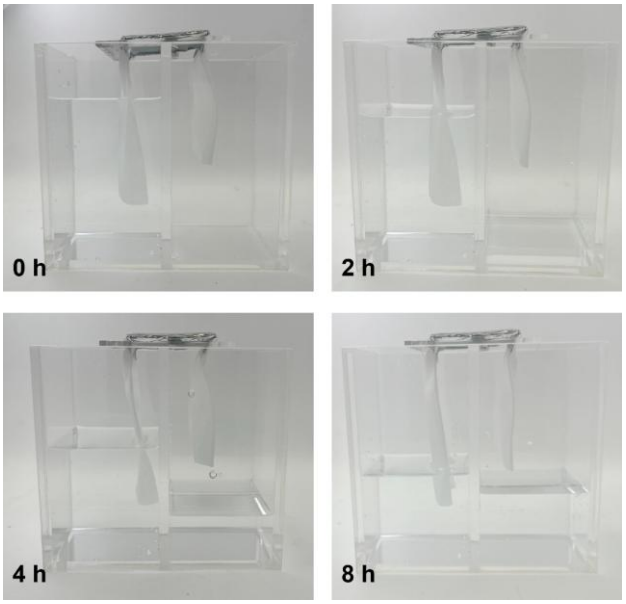

Supplementary Fig. 31 | The digital photos of seawater flow in single-stage ASP under dark conditions. The flow behavior of a multi-stage ASP under dark conditions is similar to that of a single-stage ASP.

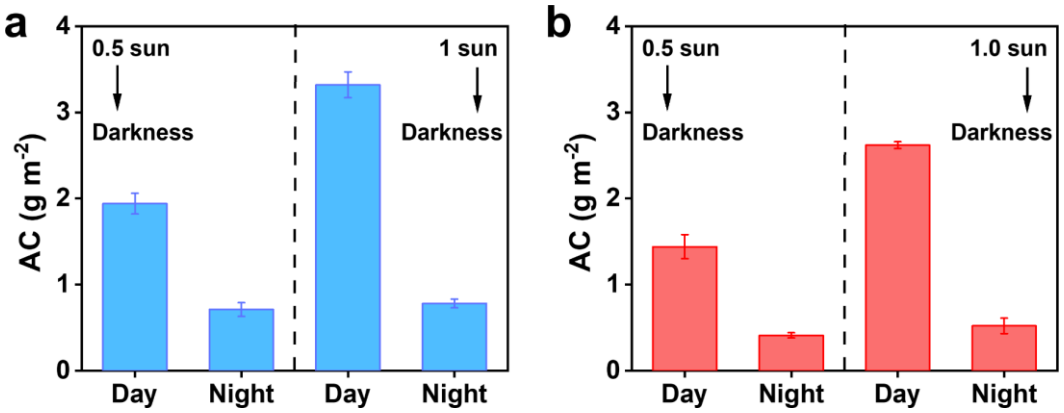

Supplementary Fig. 32 | (a) The uranium adsorption capacity and (b) the lithium adsorption capacity of parallel ASP architecture (Data are presented as mean values ± standard deviation from three independent experiments). Given that the actual outdoor average solar flux does not exceed 1 sun, the intermittent adsorption performance of ASP is evaluated only under 0.5 sun and 1 sun conditions. For the 0.5 sun test, ASP is irradiated under 0.5 sun for 8 h, after which its adsorption performance at day is calculated. The ASP is then transferred to dark conditions and maintained for 16 h, followed by evaluation of its adsorption performance at night. The 1 sun test is conducted using the same procedure. The results indicate that ASP can still adsorb target ions, albeit with reduced adsorption performance under dark conditions. In other words, the ions adsorbed on the ASP do not desorb under dark conditions. The adsorption experiments are conducted in real seawater spiked with 2.5 mg L^{-1} uranium ion or 2.5 mg L^{-1} lithium ion.

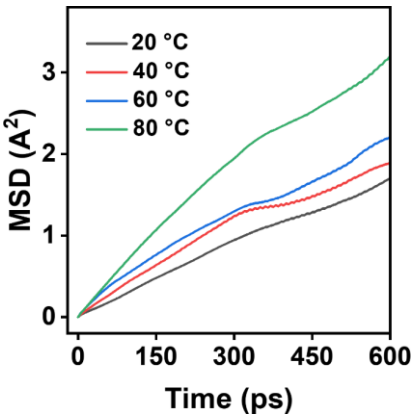

Supplementary Fig. 33 | Mean squared displacement (MSD) of UO_2^{2+} in SAU within different temperatures. Note that the slope of the curve represents the simulated diffusion coefficient. The calculation method can be found in the reported work[83].

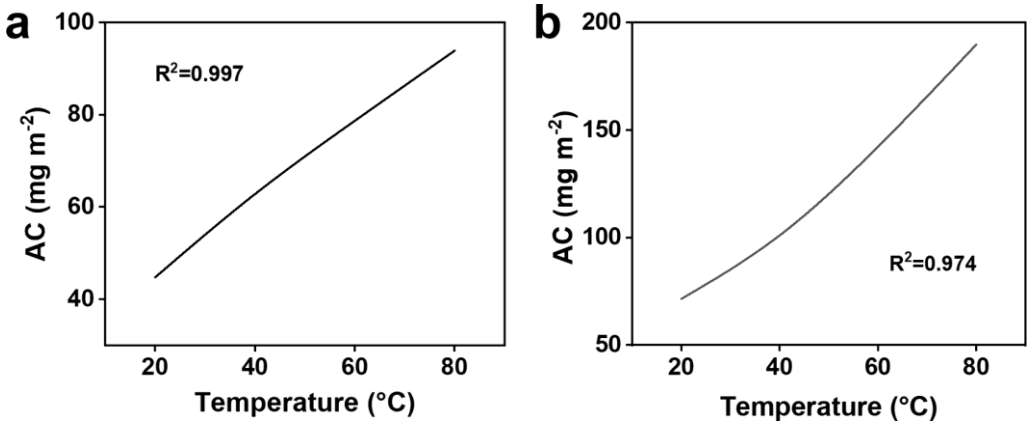

Supplementary Fig. 34 | (a) The uranium adsorption capacity of SAU; and (b) The lithium adsorption capacity of SALi under different temperature. The adsorption experiments are conducted in 2.5 mg L^{-1} uranium solution or 2.5 mg L^{-1} lithium solution.

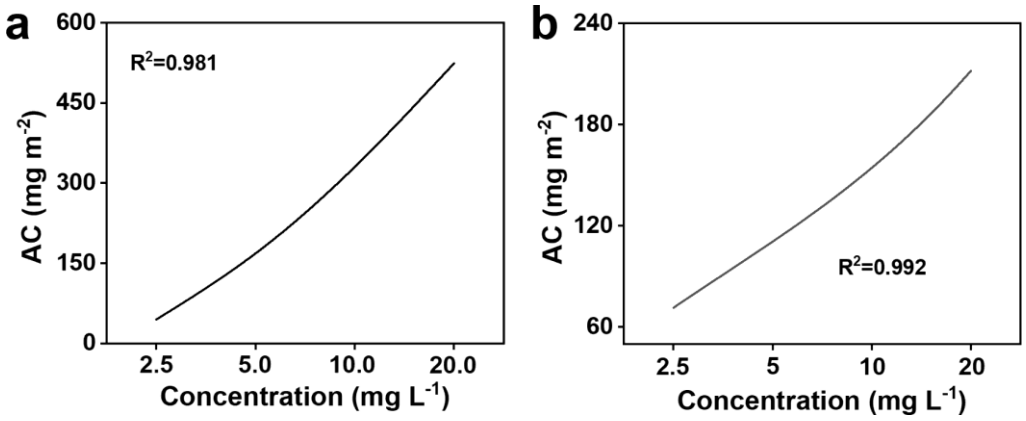

Supplementary Fig. 35 | (a) The uranium adsorption capacity of SAU; and (b) The lithium adsorption capacity of SALi under different concentration.

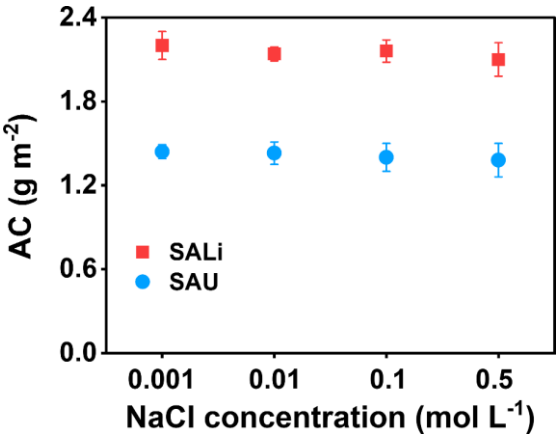

Supplementary Fig. 36 | Effect of ionic strength on the adsorption capacity of SAU and SALi (Data are presented as mean values ± standard deviation from three independent experiments). The adsorption experiments are conducted in 2.5 mg L^{-1} uranium solution or 2.5 mg L^{-1} lithium solution.

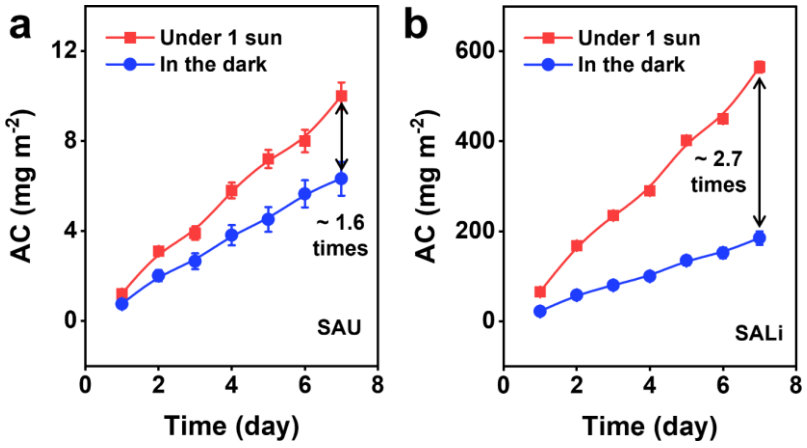

Supplementary Fig. 37 | The adsorption capacity of ASP in real seawater: (a) uranium adsorption by SAU-based ASP; and (b) lithium adsorption by SALi-based ASP (Data are presented as mean values ± standard deviation from three independent experiments).

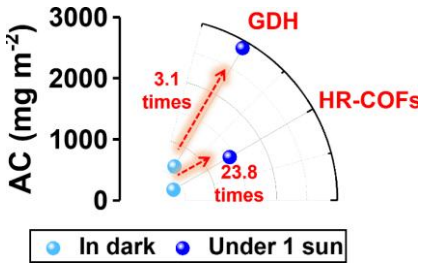

Supplementary Fig. 38 | The uranium adsorption capacity of ASP fabricated by different adsorbents: GDH[8] and HR-COFs[9]. The fabrication details are provided in Supplementary Method. The adsorption experiments are conducted in 2.5 mg L^{-1} uranium solution.

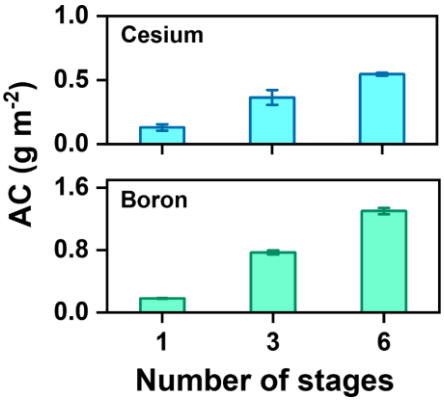

Supplementary Fig. 39 | The cesium and boron adsorption capacity of ASP fabricated by the corresponding adsorbents (Data are presented as mean values ± standard deviation from three independent experiments).

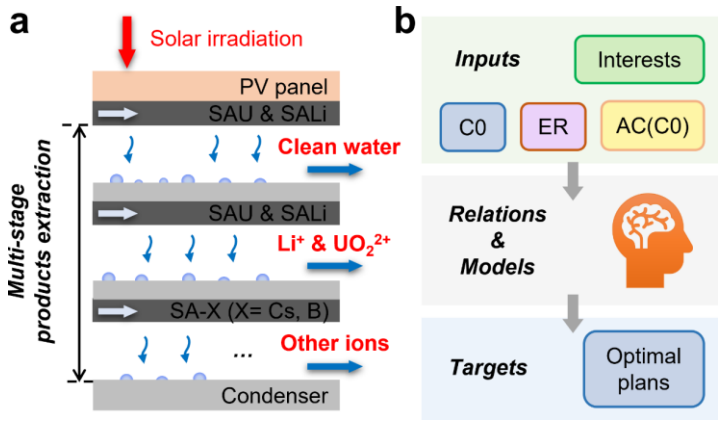

Supplementary Fig. 40 | (a) Future design of ASP for multi-product extraction; (b) Optimized design of ASP based on multi-objective optimization (such as concentration, capacity performance, and competing ions, etc).

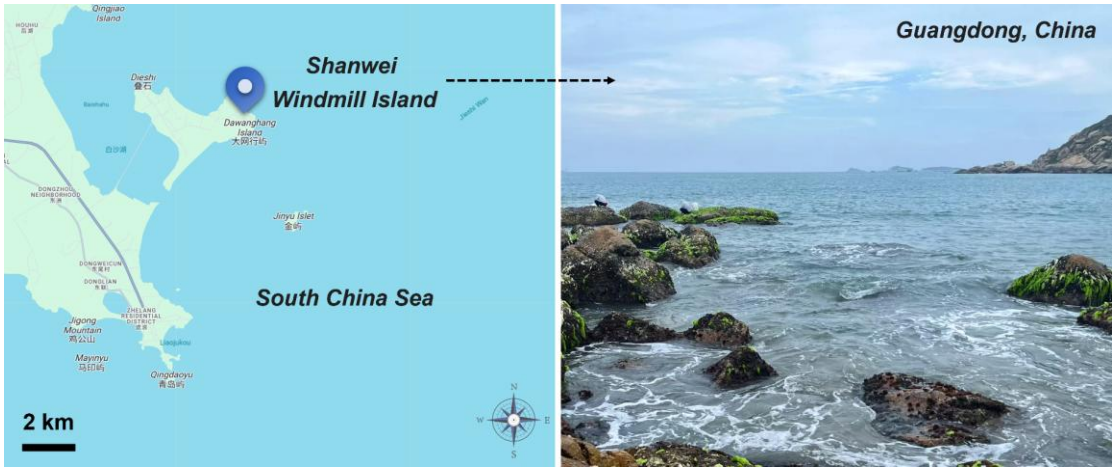

Supplementary Fig. 41 | Seawater sampling points in outdoor experiments.

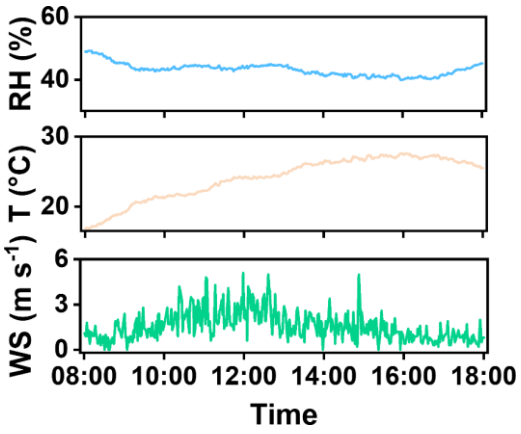

Supplementary Fig. 42 | The outdoor weather conditions. RH-relative humidity; T-ambient temperature; WS-wind speed.

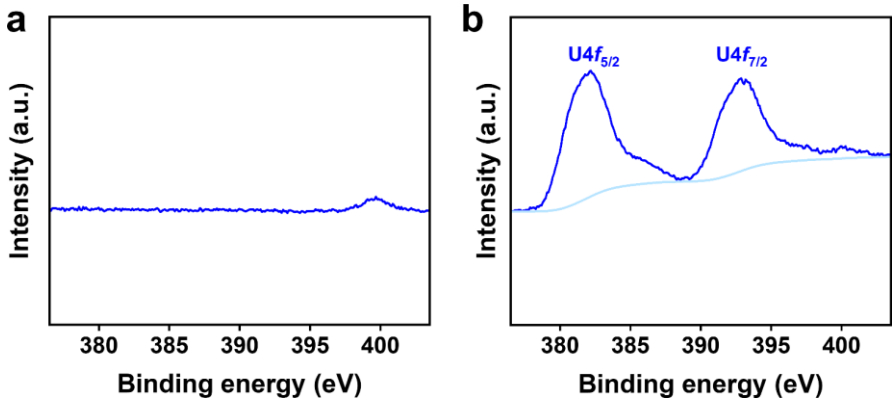

Supplementary Fig. 43 | The high-resolution XPS spectra of U4*f*: (a) SAU before and (b) after uranium adsorption.

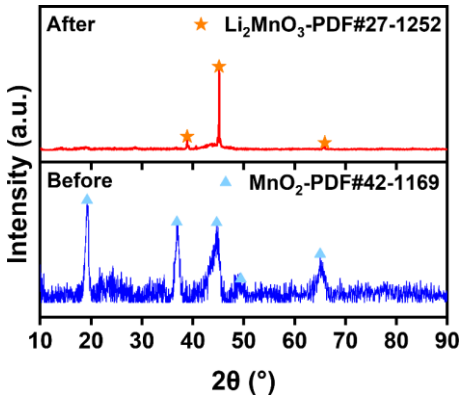

Supplementary Fig. 44 | The XRD pattern of SALi before and after lithium adsorption.

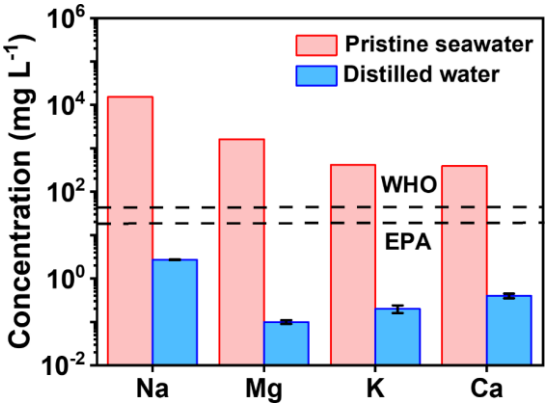

Supplementary Fig. 45 | The ion concentrations in the pristine seawater and distilled water.

Supplementary Table 1 | Comparison of ASP with representative seawater resource extraction approaches[84, 85 86, 87, 88, 89, 90]

Approach	Driving force/Energy input	Control system complexity	Mass transport/Separation mechanism	Efficiency & productivity	Key limitations under off-grid marine conditions
Electrochemistry	Continuous electrical input	High (Including electrolytic cells, pumps, etc.)	Electric-field-driven ion migration	Low under ultra-dilute conditions	High energy demand; complex control; electrode degradation; limited stability in marine off-grid environments; typically for single-resource extraction
Photochemistry	Continuous or intermittent light input	Moderate (Including adsorption reactor, pumps, etc.)	Photo-induced redox or adsorption processes	Low under ultra-dilute conditions	Material degradation; limited scalability and stability in real seawater; mainly for uranium extraction
Membrane	Continuous electrical input	Moderate to high (Including membrane module, pumps, pressure control, etc.)	Size/charge-based selective transport through membranes	Low under ultra-dilute conditions	Membrane fouling; limited selectivity in complex ionic matrices; non-negligible energy demand; typically for single-resource extraction

Adsorption	Passive or low external energy	Moderate (Including adsorption reactor, pumps, etc.)	Diffusion-limited selective adsorption	Low to moderate under ultra-dilute conditions	Sluggish kinetics; incomplete active-site utilization; potential material degradation in multi cycles; typically for single-resource extraction
ASP (this work)	Continuous or intermittent light input	Moderate to high (Including passive evaporator, PV panel, etc.)	Evaporation-induced capillary flow + selective adsorption	Moderate under ultra-dilute conditions	Currently limited by adsorption material selectivity and long-term durability

Supplementary Table 2 | The performance comparison of SAU and SALi-based single-stage ASP.

Performance indicators	**Solar flux**	**SAU**	**SALi**
Evaporation flux ($kg\ m^{-2}\ h^{-1}$)	0.5 sun	0.88	0.84
	1.0 sun	1.75	1.73
	1.5 sun	2.72	2.70
Water production rate ($kg\ m^{-2}\ h^{-1}$)	0.5 sun	0.62	0.63
	1.0 sun	1.26	1.24
	1.5 sun	1.84	1.87
PV output (mW)	0.5 sun	63.2	61.8
	1.0 sun	124.6	125.4
	1.5 sun	186.1	185.7
Evaporation enthalpy ($MJ\ kg^{-1}$)	-	1.71	1.68

Supplementary Table 3 | The TOC, TDS, and pH value of condensed water.

	TOC ($mg\ L^{-1}$)	TDS ($mg\ L^{-1}$)	pH
1st cycle	1.8	2.7	7.2
5th cycle	1.6	2.4	7.2
10th cycle	1.7	2.3	7.1

Supplementary Table 4 | The adsorption capacity and temperature of every chamber's capillary wick in the 6-stage ASP when operating in natural seawater for 7 days under 1 sun (Data are presented as mean values ± standard deviation from three independent experiments)...

i	Temperature (°C)	Uranium adsorption capacity (mg m^{-2})	Lithium adsorption capacity (mg m^{-2})
1	42.6 ± 0.02	2.9 ± 0.05	173.1 ± 2.7
2	38.9 ± 0.01	1.9 ± 0.04	113.2 ± 3.3
3	35.1 ± 0.06	1.7 ± 0.08	94.5 ± 1.5
4	32.4 ± 0.04	1.4 ± 0.04	69.8 ± 2.4
5	29.8 ± 0.02	1.0 ± 0.17	61.8 ± 4.4
6	27.5 ± 0.04	0.8 ± 0.22	51.8 ± 0.3

Supplementary Table 5 | Lithium separation performance of ASP from other cations in natural seawater (Some data are presented as mean values ± standard deviation from three independent experiments).

Cations	C_0 (mmol L^{-1})	C_e (mmol L^{-1})	AC (mmol m^{-2})	q_e (mmol g^{-1} HMO)	α_{Me}^{Li}
Li	~ 0.026	~ 0.004	4.50 ± 0.02	0.177 ± 0.002	1
Na	~ 462.2	~ 462.198	0.48 ± 0.03	0.018 ± 0.002	~ 1.08×10^6
K	~ 10.3	~ 10.298	0.37 ± 0.01	0.015 ± 0.002	~ 3.13×10^4
Mg	~ 53.1	~ 53.097	0.56 ± 0.17	0.022 ± 0.006	~ 1.07×10^5
Ca	~ 9.8	~ 9.798	0.47 ± 0.02	0.018 ± 0.001	~ 2.35×10^4

Supplementary Table 6 | Uranium separation performance of ASP from other cations in natural seawater (Some data are presented as mean values ± standard deviation from three independent experiments).

Cations	C_0 (μmol L^{-1})	C_e (μmol L^{-1})	AC (μmol m^{-2})	q_e (μmol g^{-1} PPC)	α_{Me}^{U}
U	~ 0.014	~ 0.0013	2.63 ± 0.04	0.103 ± 0.006	1
V	~ 0.037	~ 0.0354	0.33 ± 0.03	0.013 ± 0.005	~ 204
Fe	~ 0.010	~ 0.007	0.49 ± 0.05	0.019 ± 0.007	~ 30.1
Ni	~ 0.008	~ 0.007	0.08 ± 0.03	0.003 ± 0.005	~ 190
Cu	~ 0.004	~ 0.003	0.23 ± 0.04	0.009 ± 0.006	~ 24.1
Zn	~ 0.008	~ 0.006	0.31 ± 0.03	0.012 ± 0.005	~ 40.6

Supplementary Table 7 | The extraction cost of ASP.

Items	Final extraction cost	Normalized extraction cost
Electricity	US$ 16.85	US$ 0.0589 $(kW\ h)^{-1}$
Clean water	US$ 4.67	US$ 0.00084 kg^{-1}
$UO_2CO_3 \cdot Na_2CO_3$	US$ 0.055	US$ 136 kg^{-1}
LiCl	US$ 0.454	US$ 8.49 kg^{-1}

Supplementary Table 8 | The LCA impact indicators of electricity, freshwater, lithium chloride, and uranium product generated by ASP.

Product	Indicator	Value per kW h
Electricity	GWP	41 g CO_2-eq
	PED	0.52 MJ
	WC	1.26 L
	EP	5.1×10^{-5} kg PO_4-eq
	HTP	0.014 kg 1,4-DCB-eq
Product	**Indicator**	**Value per m^3**
Clean water	GWP	3.3 kg CO_2-eq
	PED	41 MJ
	WC	100 L
	EP	4.0×10^{-3} kg PO_4-eq
	HTP	1.1 kg 1,4-DCB-eq
Product	**Indicator**	**Value per kg**
LiCl	GWP	5.9 kg CO_2-eq
	PED	75 MJ
	WC	180 L
	EP	7.7×10^{-3} kg PO_4-eq
	HTP	2.1 kg 1,4-DCB-eq
Product	**Indicator**	**Value per kg**
$UO_2CO_3 \cdot Na_2CO_3$	GWP	95 kg CO_2-eq
	PED	1200 MJ
	WC	280 L
	EP	0.12×10^{-3} kg PO_4-eq
	HTP	33 kg 1,4-DCB-eq

Reference

1. Yu Z, Su Y, Gu R, Wu W, Li Y, Cheng S. Micro-nano water film enabled high-performance interfacial solar evaporation. *Nano-Micro Lett.* **15**, 214 (2023).
2. Yan W*, et al.* Facile solid-phase method for preparing a highly active and stable PtZn-based oxygen reduction/hydrogen evolution bifunctional electrocatalyst: Effect of bi-facet lattice strain on catalytic activity. *ACS Appl. Energy Mater.* **5**, 13791-13801 (2022).
3. Tang L*, et al.* Highly efficient, stable, and recyclable hydrogen manganese oxide/cellulose film for the extraction of lithium from seawater. *ACS Appl. Mater. Interfaces* **12**, 9775-9781 (2020).
4. Li C, Zhan H, Qiao Y, Shi C, Qian Z, Liu Z. Constructing porous hydrophilic HMO/CTA@PDA composite hydrogel for super-high and ultrafast extraction of lithium ions. *Desalination* **593**, 118216 (2025).
5. Xia Q*, et al.* Solar-enhanced lithium extraction with self-sustaining water recycling from salt-lake brines. *Proc. Natl. Acad. Sci.* **121**, e2400159121 (2024).
6. Chen K, Li L, Li B, Yang Y, Zhu K, Zhang J. Simultaneous fresh water collection and Li^+ selective adsorption enabled by a salt-resistant separated solar evaporator. *Adv. Funct. Mater.* **34**, 2402221 (2024).
7. Li T*, et al.* Photothermal-enhanced uranium extraction from seawater: a biomass solar thermal collector with 3D ion-transport networks. *Adv. Funct. Mater.* **33**, 2212819 (2023).
8. Liang H, Mu Y, Yin M, He P-P, Guo W. Solar-powered simultaneous highly efficient seawater desalination and highly specific target extraction with smart DNA hydrogels. *Sci. Adv.* **9**, eadj1677 (2023).
9. Yuan Y*, et al.* High-capacity uranium extraction from seawater through constructing synergistic multiple dynamic bonds. *Nat. Water* **3**, 89-98 (2025).
10. Li L, Yu Z, Jin B, Yu X, Su Y, Cheng S. Hierarchical photothermal network spontaneously facilitates co-extraction of clean water and boron. *Adv. Funct. Mater.* **35**, 2505776 (2025).

11. Zhu L*, et al.* Solar-powered hierarchical microenvironments with authigenic multi-field synergies for simultaneous extraction of freshwater and cesium. *Adv. Sci.* **12**, 2505997 (2025).
12. Yu Z*, et al.* Intensifying the co-production of vapor and salts by a one-way brine-flowing structure driven by solar irradiation or waste heat. *Desalination* **539**, 115942 (2022).
13. Tzeng G-H, Huang J-J. *Multiple attribute decision making: methods and applications*. CRC press (2011).
14. Kumar A*, et al.* A sustainable rural electrification based on a socio-techno-economic-environmental-political microgrid design framework. *Energy Environ. Sci.* **15**, 4213-4246 (2022).
15. Tang J*, et al.* All-natural 2D nanofluidics as highly-efficient osmotic energy generators. *Nat. Commun.* **15**, 3649 (2024).
16. Heidari A, Boleydei H, Rohani A, Lu HR, Younesi H. Integrating life cycle assessment and life cycle costing using TOPSIS to select sustainable biomass-based -carbonaceous adsorbents for CO_2 capture. *J. Clean. Prod.* **357**, 131968 (2022).
17. Behzadian M, Khanmohammadi Otaghsara S, Yazdani M, Ignatius J. A state-of the-art survey of TOPSIS applications. *Expert Syst. Appl.* **39**, 13051-13069 (2012).
18. Qian Y*, et al.* Highly efficient uranium adsorption by salicylaldoxime/polydopamine graphene oxide nanocomposites. *J. Mater. Chem. A.* **6**, 24676-24685 (2018).
19. Liu F, Luo Y, Hu B. Simultaneous elimination of U (VI) and Eu (III) by phytic acid decorated MXenes@MOFs composites in water: Performance, kinetics and mechanism. *Sep. Purif. Technol.* **327**, 124912 (2023).
20. Peng Q, Jin T, Wang C, Qian Y. Phytic acid-modified carboxymethyl cellulose hydrogel for uranium adsorption from aqueous solutions. *Int. J. Biol. Macromol.* **256**, 128545 (2024).
21. Tan L*, et al.* Enhanced adsorption of uranium (VI) using a three-dimensional

layered double hydroxide/graphene hybrid material. *Chem. Eng. J.* **259**, 752-760 (2015).

22. Liu F, Hu J, Hu B. Magnetic MXene-NH_2 decorated with persimmon tannin for highly efficient elimination of U (VI) and Cr (VI) from aquatic environment. *Int. J. Biol. Macromol.* **219**, 886-896 (2022).
23. Zhu J*, et al.* Graphene oxide based ion-imprinted polymers for selective uranium adsorption from seawater. *Appl. Surf. Sci.* **640**, 158378 (2023).
24. Tian Y*, et al.* Synthesis of phosphorylated hyper-cross-linked polymers and their efficient uranium adsorption in water. *J. Hazard. Mater.* **419**, 126538 (2021).
25. Su X*, et al.* Phytate-modified MOFs grown on carbon nanotubes for efficient adsorption of uranium (VI) from seawater. *Sep. Purif. Technol.* **335**, 126102 (2024).
26. Chaudhary M, Singh L, Rekha P, Srivastava VC, Mohanty P. Adsorption of uranium from aqueous solution as well as seawater conditions by nitrogen-enriched nanoporous polytriazine. *Chem. Eng. J.* **378**, 122236 (2019).
27. Xin Q*, et al.* Mechanism of selective uranium adsorption using polyvinyl alcohol/Cyphos IL-101/reduced graphene oxide composites. *Chem. Eng. J.* **500**, 157256 (2024).
28. Li S*, et al.* Graphene oxide based dopamine mussel-like cross-linked polyethylene imine nanocomposite coating with enhanced hexavalent uranium adsorption. *J. Mater. Chem. A.* **7**, 16902-16911 (2019).
29. Qin X, Yang W, Yang Y, Gu D, Guo D, Pan Q. A zinc metal-organic framework for concurrent adsorption and detection of uranium. *Inorg. Chem.* **59**, 9857-9865 (2020).
30. Zhu R*, et al.* "Three-dimensional environment-friendly" amino acid functionalized chitosan: Uranium adsorption performance and mechanism research. *Carbohydr. Polym.* **343**, 122464 (2024).
31. Li M, Liu H, Chen T, Dong C, Sun Y. Synthesis of magnetic biochar composites for enhanced uranium (VI) adsorption. *Sci. Total Environ.* **651**, 1020-1028

(2019).

32. Xin Q*, et al.* Mechanism for the seleikctive adsorption of uranium from seawater using carboxymethyl-enhanced polysaccharide-based amidoxime adsorbent. *Carbohydr. Polym.* **324**, 121576 (2024).

33. Wang Y, Lu Z, Luo M, Zhao Z, Wei Y, Wang H. Enhanced uranium adsorption performance of porous MXene nanosheets. *Sep. Purif. Technol.* **335**, 126134 (2024).

34. Chen Z*, et al.* Synthesis of magnetic Fe_3O_4/CFA composites for the efficient removal of U (VI) from wastewater. *Chem. Eng. J.* **320**, 448-457 (2017).

35. Zhang G*, et al.* Synthesis of amino acid modified MIL-101 and efficient uranium adsorption from water. *J Mol Liq* **349**, 118095 (2022).

36. Zeng J*, et al.* New amidoxime-based material TMP-g-AO for uranium adsorption under seawater conditions. *Ind. Eng. Chem. Res.* **56**, 5021-5032 (2017).

37. Fan F-L*, et al.* Rapid removal of uranium from aqueous solutions using magnetic Fe_3O_4@ SiO_2 composite particles. *J. Environ. Radioact.* **106**, 40-46 (2012).

38. Wang Y*, et al.* Ultra-high mechanical property and multi-layer porous structure of amidoximation ethylene-acrylic acid copolymer balls for efficient and selective uranium adsorption from radioactive wastewater. *Chemosphere* **280**, 130722 (2021).

39. He Y*, et al.* A novel phosphorylated hyper-crosslinked porous polymer for efficient uranium adsorption in water. *Sep. Purif. Technol.* **330**, 125448 (2024).

40. Lu S*, et al.* Spectroscopic and modeling investigation of efficient removal of U (VI) on a novel magnesium silicate/diatomite. *Sep. Purif. Technol.* **174**, 425-431 (2017).

41. Su Y, Gu R, Li Y, Wu W, Yu Z, Cheng S. Seawater interfacial evaporation in composite gel enables photovoltaic cooling, simultaneous seawater desalination, and enhanced uranium extraction. *Adv. Funct. Mater.* **36**, 2420651 (2025).

42. Li Y*, et al.* Design and synthesis of a novel bifunctional polymer with

malonamide and carboxyl group for highly selective separation of uranium (VI). *Sep. Purif. Technol.* **302**, 122115 (2022).

43. Zhu M*, et al.* Efficient uranium adsorption by amidoximized porous polyacrylonitrile with hierarchical pore structure prepared by freeze-extraction. *J Mol Liq* **328**, 115304 (2021).
44. Chitrakar R, Makita Y, Ooi K, Sonoda A. Synthesis of iron-doped manganese oxides with an ion-sieve property: lithium adsorption from Bolivian brine. *Ind. Eng. Chem. Res.* **53**, 3682-3688 (2014).
45. Qian F, Guo M, Qian Z, Li Q, Wu Z, Liu Z. Highly lithium adsorption capacities of $H_{1.6}Mn_{1.6}O_4$ ion-sieve by ordered array structure. *ChemistrySelect* **4**, 10157-10163 (2019).
46. Liu Z, Chen K, Ding J, Wang W, Lu J. The modification of $MnO_2{\cdot}0.5H_2O$ by Al/Mg doping to enhance lithium adsorption and reduce manganese dissolution with application to brines. *Hydrometallurgy* **219**, 106078 (2023).
47. Zhu X, Yue H, Sun W, Zhang L, Cui Q, Wang H. Study on adsorption extraction process of lithium ion from West Taijinar brine by shaped titanium-based lithium ion sieves. *Sep. Purif. Technol.* **274**, 119099 (2021).
48. Xiao J, Nie X, Sun S, Song X, Li P, Yu J. Lithium ion adsorption-desorption properties on spinel $Li_4Mn_5O_{12}$ and pH-dependent ion-exchange model. *Adv Powder Technol* **26**, 589-594 (2015).
49. Wang S, Li P, Zhang X, Zheng S, Zhang Y. Selective adsorption of lithium from high Mg-containing brines using H_xTiO_3 ion sieve. *Hydrometallurgy* **174**, 21-28 (2017).
50. Li X, Tao B, Jia Q, Guo R. Preparation and adsorption performance of multi-morphology $H_{1.6}Mn_{1.6}O_4$ for lithium extraction. *Chin J Chem Eng* **34**, 68-76 (2021).
51. Sun J*, et al.* Preparation of high hydrophilic H_2TiO_3 ion sieve for lithium recovery from liquid lithium resources. *Chem. Eng. J.* **453**, 139485 (2023).
52. Gao J-m, Du Z, Zhao Q, Guo Y, Cheng F. Enhanced Li^+ adsorption by magnetically recyclable iron-doped lithium manganese oxide ion-sieve:

Synthesis, characterization, adsorption kinetics and isotherm. *J. Mater. Res. Technol.* **13**, 228-240 (2021).

53. Li X*, et al.* Taming wettability of lithium ion sieve via different TiO_2 precursors for effective Li recovery from aqueous lithium resources. *Chem. Eng. J.* **392**, 123731 (2020).

54. Wang Y, Zhang X, Zhao X, Liu Y, Wu D, Huang H. Tailoring carboxyl-rich micro-environment of metal-organic framework via mixed linkers strategy for enhanced adsorption of lithium ion. *Chem. Eng. J.* **511**, 162116 (2025).

55. Li X*, et al.* Highly selective separation of lithium with hierarchical porous lithium-ion sieve microsphere derived from MXene. *Desalination* **537**, 115847 (2022).

56. Luo Q, Dong M, Li Q, Wu Z, Liu Z, Li J. Improve the durability of lithium adsorbent Li/Al-LDHs by Fe^{3+} substitution and nanocomposite of FeOOH. *Miner Eng* **185**, 107717 (2022).

57. Xiao X, Li J, Qiu K, Chen M, Zhang X. Dual surfactants-assisted adsorption of lithium ions in liquid lithium resources on a superhydrophilic spinel-type $H_4Ti_5O_{12}$ ion sieve. *Sep. Purif. Technol.* **330**, 125479 (2024).

58. Gao Y, Wang S, Gao F, Guo C, Dong J, Chen G. Al and Cr ions co-doped spinel manganese lithium ion-sieve with enhanced Li^+ adsorption performance and structural stability. *Microporous Mesoporous Mater* **351**, 112492 (2023).

69. Huang Y, Wang R. An efficient lithium ion imprinted adsorbent using multi-wall carbon nanotubes as support to recover lithium from water. *J. Clean. Prod.* **205**, 201-209 (2018).

60. Kamran U, Heo Y-J, Lee JW, Park S-J. Chemically modified activated carbon decorated with MnO_2 nanocomposites for improving lithium adsorption and recovery from aqueous media. *J Alloys Compd* **794**, 425-434 (2019).

61. Bao L-R, Zhang J-Z, Tang W-P, Sun S-Y. Synthesis and adsorption properties of metal oxide-coated lithium ion-sieve from salt lake brine. *Desalination* **546**, 116196 (2023).

62. Shin J*, et al.* Recovery of Li from seawater using $Li_{1.33}Mn_{1.67}O_4$ immobilized

multi-stage column system. *Desalination* **583**, 117656 (2024).

63. Kamran U, Park S-J. Hybrid biochar supported transition metal doped MnO_2 composites: Efficient contenders for lithium adsorption and recovery from aqueous solutions. *Desalination* **522**, 115387 (2022).

64. Xu N, Li S, Guo M, Qian Z, Li W, Liu Z. Synthesis of $H_4Mn_5O_{12}$ nanotubes lithium ion sieve and its adsorption properties for Li^+ from aqueous solution. *ChemistrySelect* **4**, 9562-9569 (2019).

65. Wang X*, et al.* Novel C-PDA adsorbents with high uptake and preferential adsorption of ethane over ethylene. *Chem Eng Sci* **155**, 338-347 (2016).

66. Saif F, Yaseen S, Alameen A, Mane S, Undre P. Identification and characterization of Aspergillus species of fruit rot fungi using microscopy, FT-IR, Raman and UV-Vis spectroscopy. *Spectrochim. Acta, Part A* **246**, 119010 (2021).

67. Sun T, Li Zj, Wang Hg, Bao D, Meng Fl, Zhang Xb. A biodegradable polydopamine-derived electrode material for high-capacity and long-life lithium-ion and sodium-ion batteries. *Angew. Chem. Int. Ed.* **55**, 10662-10666 (2016).

68. Zhu D*, et al.* Investigation of magnesium hydroxide functionalized by polydopamine/transition metal ions on flame retardancy of epoxy resin. *J Therm Anal Calorim* **147**, 13301-13312 (2022).

69. Sharma S, Lee J, Dang TT, Hur SH, Choi WM, Chung JS. Ultrathin freestanding PDA-Doped rGO/MWCNT composite paper for electromagnetic interference shielding applications. *Chem. Eng. J.* **430**, 132808 (2022).

70. Xie Y, Zheng Y, Fan J, Wang Y, Yue L, Zhang N. Novel electronic–ionic hybrid conductive composites for multifunctional flexible bioelectrode based on in situ synthesis of poly (dopamine) on bacterial cellulose. *ACS Appl. Mater. Interfaces* **10**, 22692-22702 (2018).

71. Chen X*, et al.* Polyacrylamide/sodium alginate/sodium chloride photochromic hydrogel with high conductivity, anti-freezing property and fast response for information storage and electronic skin. *Int. J. Biol. Macromol.* **268**, 131972

(2024).

72. Xie Y*, et al.* Efficient electromagnetic wave absorption performances dominated by exchanged resonance of lightweight PC/Fe_3O_4@PDA hybrid nanocomposite. *Chem. Eng. J.* **457**, 141205 (2023).

73. Mo L, Pang H, Tan Y, Zhang S, Li J. 3D multi-wall perforated nanocellulose-based polyethylenimine aerogels for ultrahigh efficient and reversible removal of Cu (II) ions from water. *Chem. Eng. J.* **378**, 122157 (2019).

74. Zhang P*, et al.* Photoisomerization-mediated tunable pore size in metal organic frameworks for U(VI)/V(V) selective separation. *Nat. Commun.* **16**, 2361 (2025).

75. Shimura S, Herrero R, Zuffo MK, Baesso Grimoni JA. Production costs estimation in photovoltaic power plants using reliability. *Sol. Energy* **133**, 294-304 (2016).

76. Walker, H., et al. *Model of operation-and-maintenance costs for photovoltaic systems*. National Renewable Energy Lab. (NREL), Golden, CO, USA, 2020.

77. Zhang Q*, et al.* Biological fermentation pilot-scale systems and evaluation for commercial viability towards sustainable biohydrogen production. *Nat. Commun.* **15**, 4539 (2024).

78. Peng Y, Yang J, Deng C, Deng J, Shen L, Fu Y. Acetolysis of waste polyethylene terephthalate for upcycling and life-cycle assessment study. *Nat. Commun.* **14**, 3249 (2023).

79. 12 IPT. Environmental Life Cycle Assessment of PV Systems-2023 Fact Sheet. (2023).

80. Nugent D, Sovacool BK. Assessing the lifecycle greenhouse gas emissions from solar PV and wind energy: A critical meta-survey. *Energy Policy* **65**, 229-244 (2014).

81. Zhang M, Yu S, Shi C, Wang H, Chang N. Carbon footprint analysis and carbon neutrality potential of desalination by reverse osmosis for different applications basd on life cycle assessment method. *Sci. Rep.* **15**, 40842 (2025).

82. Schenker V, Pfister S. Current and future impacts of lithium carbonate from

brines: A global regionalized life cycle assessment model. *Environ. Sci. Technol.* **59**, 6543-6555 (2025).

83. El Kaim Billah R, et al. Experimental and theoretical studies on nitrate removal using epichlorohydrin-modified cross-linked chitosan derived from shrimp waste. *Environ. Sci. Pollut. Res* **30**, 107772-107789 (2023).

84. Yu J, Wang R, Xu Z. Toward water- and energy-sustainable lithium extraction from brines. *Joule* **10**, 102270 (2026).

85. Wang Y*, et al.* Bipolar electrochemical uranium extraction from seawater with ultra-low cell voltage. *Nat. Sustain.* **8**, 682-691 (2025).

86. Wang Y*, et al.* Designing self-adaptative cyclized polyacrylonitrile-polyethyleneimine conjugates enhance uranium extraction from natural seawater. *Nat. Commun.* **16**, 9249 (2025).

87. Yu Z*, et al.* Adsorption-responsive bionic photothermal ion pump for reversible seawater lithium extraction. *Nat. Commun.* **16**, 8825 (2025).

88. Xie Y*, et al.* Uranium extraction from seawater: material design, emerging technologies and marine engineering. *Chem. Soc. Rev.* **52**, 97-162 (2023).

89. Zhu L*, et al.* Solar-powered hierarchical microenvironments with authigenic multi-field synergies for simultaneous extraction of freshwater and cesium. *Adv. Sci.* **12**, 2505997 (2025).

90. Li S*, et al.* Solar-driven multi-field synergistic strategy for integrated freshwater production and boron harvesting. *Sci. Bull.* **71**, 566-576 (2026).